A General Model to Optimise Cu^{II} Labelling Efficiency of Double-Histidine Motifs for Pulse Dipolar EPR Applications

Joshua L. Wort,[a] Katrin Ackermann,[a] David G. Norman,[b] and Bela E. Bode*[a]

(a) EaStCHEM School of Chemistry, Biomedical Sciences Research Complex, and Centre of Magnetic Resonance, University of St Andrews North Haugh, St Andrews KY16 9ST (UK)

(b) School of Life Sciences, University of Dundee, Medical Sciences Institute, Dundee, DD1 5EH (UK)

Table of Contents

I   **Experimental Procedures:**

1.1   Pulse EPR Sample Preparation:

All material was exchanged into deuterated buffer A (42.4 mM Na_2HPO_4, 7.6 mM KH_2PO_4, 150 mM NaCl, pH 7.4) by first freeze-drying and then re-dissolving in D_2O. For X-band PELDOR samples of 6H/8H/28R1 and 6R1/28H/32H GB1 constructs, a total volume of 15 µL was used. All EPR samples were frozen by direct immersion into liquid nitrogen. Cu^{II}-IDA and Cu^{II}-NTA stock solutions were prepared as previously described; and for Cu^{II}-labelling, Cu^{II}-IDA and Cu^{II}-NTA stock solutions with nominal concentrations of 100 and 10 mM were used, respectively.

1.2   Mass Spectrometry:

All mass spectra were collected in-house using a Sciex Matrix Assisted Laser Desorption/Ionisation (MALDI) TOF/TOF 4800 mass-spectrometer, with samples crystallised using a matrix of α-cyano-4-hydroxycinnamic acid. I6H/N8H/K28H/Q32H GB1 samples were submitted at 20 µM in buffer A, and mass spectra were recorded in the absence of Cu^{II}-labels.

1.3   EPR Instrumentation:

All pulse EPR experiments were performed using a Bruker ELEXSYS 580 pulse EPR spectrometer. Temperatures were maintained using a cryogen-free variable temperature cryostat (Cryogenic Ltd) operating in the 1.8-300 K temperature range. All measurements of the electron spin longitudinal relaxation times (T_1), and transverse dephasing times (T_m) of Cu^{II}-IDA and Cu^{II}-NTA, and all 5-pulse dead-time free RIDME measurements[1] were performed at 30 K, using a high-power 150 W travelling-wave tube (TWT; Applied Systems Engineering) at Q-band (34 GHz) in a critically coupled 3 mm cylindrical resonator (Bruker ER 5106QT-2w in TE012 mode). All 4-pulse dead-time free Pulse Electron-electron Double Resonance (PELDOR) measurements[2] were performed at 10 K at X-band (9.4 GHz) with a 1 kW TWT (Applied Systems Engineering) in an over-coupled 3 mm split-ring resonator (Bruker 4118X-MS3), unless otherwise stated.

1.4   The 5-pulse RIDME Experiment and Measurement Parameters:

The 5-pulse RIDME pulse sequence[1] is shown below in figure S1. As stated in the main text all RIDME measurements were performed detecting at the maximum of the Cu^{II}-NTA spectrum.
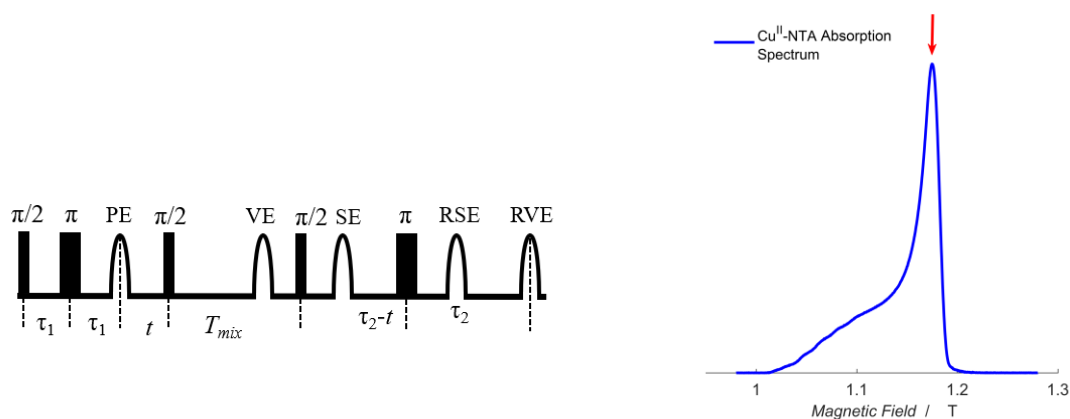
Figure S1. The 5-pulse RIDME pulse sequence and an echo-detected EPR spectrum of Cu^{II}-NTA with the detection position used in the Cu^{II}-Cu^{II} RIDME measurements indicated as a red arrow, shown in the left and right panels respectively. For the RIDME experiment the refocused virtual echo (RVE) is observed, and is modulated by the electron-electron dipolar coupling as a function of *t*. This defines the position of the third and fourth pulses, which comprise a longitudinal mixing block, separated by the fixed interval T_{mix}. The dipolar coupling manifests from intrinsic electron spin longitudinal relaxation events (Δms) during the mixing block, after which dipolar evolution occurs during the interval τ₂. The remaining echoes

generated by the sequence are indicated; primary echo (PE), stimulated echo (SE), virtual echo (VE) and refocused stimulated echo (RSE), separated by 2τ from the detected RVE.

For all measurements, rectangular pulses of lengths 12 and 24 ns (π/2 and π, respectively) were consistently used, and the detection frequency was placed at the maximum of the Cu^{II}-NTA spectrum. All acquisitions were performed over three scans (unless otherwise stated), with 10 shots per point, with a shot repetition time (SRT) of 2 ms, and deuterium ESEEM was suppressed *via* a 16-step nuclear modulation τ-averaging cycle.[3] Signal contributions from unwanted echoes were eliminated using an 8-step phase-cycle, totalling 128 steps per measurement (resulting in 384 echoes per point per scan), with the refocused virtual echo (RVE) being detected. For all samples, at least two lengths of mixing block were recorded; a short reference mixing time (T_{ref}) and a long mixing time (T_{mix}) to allow suppression and observation of the dipolar coupling, respectively. A pseudo-titration series (a titration with discrete samples prepared for each data point in the series) of I6H/N8H/K28H/Q32H GB1 was measured at 100 μM protein concentration, in presence of varying Cu^{II}-NTA concentration. All RIDME data was used without division by the reference trace and background corrected using stretched exponential functions with stretching exponent bounded between 1 and 2, unless otherwise stated.

1.5   5-pulse RIDME Data Processing, Analysis and Validations:

All 5-pulse RIDME traces were processed using DeerAnalysis2018, and were background-corrected using either second order polynomial or stretched-exponential functions as specified in the text, and the observed modulation depth quotients were found to be robust against background correction models. The stretched exponential functions were of the form:[4]

$$y = c \times \exp\left(-(k \times t)^{\frac{d}{3}}\right) \hspace{5cm} (S1)$$

Where c is the initial amplitude, k is the decay constant, t is the time-point, and d is the background dimension, which is constrained between 3 and 6, in keeping with recent RIDME theory.[5] For the validations of the RIDME traces (see ESI), a modified version of the Tikhonov validation functionality in DeerAnalysis2018[6] was used; a total of 896 trials were performed for each validation, consisting of 16 white-noise iterations (noise-level of 1.5), 8 iterations of background start position (between 5-30% of the total RIDME trace length), and 7 iterations of background dimension (between 3-6 in increments of 0.5). All validation trials were pruned (prune level = 1.15), and for each trial remaining after pruning, a modulation depth (Δ) was calculated. The standard deviation (σ) is then used to approximate the modulation depth error, relevant in the propagation of errors to calculate K_D from RIDME pseudo-titration series. Bivariate fitting used in-house Matlab scripts and employed a Nelder-Mead simplex. Each K_D value was varied independently, and a least-squares bivariate error minimisation was performed. The root-mean square deviation (RMSD) was used as an estimate of goodness-of-fit between simulation and experiment. Fits were found to be largely stable regardless of chosen initial parameters.

It should be noted that distance distributions are based on the dipolar coupling calculated for the free electron *g*-value and this has not been corrected throughout the manuscript. If the distributions were analyzed and interpreted in detail the x-axes would need to be scaled by a factor 0.885.[7] Furthermore, background imperfections from using a short $τ_1$ were compensated by dividing by reference traces and did not hamper modulation depth analysis.[4]

1.6   Electron Spin-echo Decay and Inversion Recovery Measurement Parameters:

The 2-pulse electron spin-echo decay (ESE) experiment (π/2-τ-π) was applied at the maximum field position of the Cu^{II}-chelate spectrum, using 16 and 32 ns π/2- and π-pulses. Traces were acquired with a trace length of 20 or 33 μs as stated, measured at 30 K, using a τ of 800 ns (due to increased dead-time in high Q mode), which was incremented in steps of 8 ns, for 4096 points. For all measurements, an SRT of 2 ms was used. Raw data were fitted using a stretched-exponential function to estimate T_m:

$$y = A_0 \left[exp\left(\left(\frac{-\tau}{T_m}\right)^x\right) \right]$$
(S2)

The 3-pulse inversion recovery (IR) experiment (π-T-π/2-τ-π) was used and applied at the maximum field position of the Cu^{II}-chelate spectrum with a 12 ns inversion pulse (nominal flip-angle π). 20 and 40 ns pulses (π/2- and π, respectively) were used for the observer subsequence (unless otherwise stated). Traces were acquired to 500 μs and the time interval T was incremented in steps of 200 ns, using an SRT of 2 ms (unless otherwise stated) and a τ of 800 ns. Raw data were fitted with mono- and bi-exponential functions, to estimate T_1:

$$y = A_0 \left[1 - 2a \times exp\left(\frac{-x}{T_1}\right) \right]$$
(S3)

$$y = A_0 \left[1 - 2a \left(b \times exp\left(\frac{-x}{T_{1B\ slow}}\right) + (1-b) \times exp\left(\frac{-x}{T_{1B\ fast}}\right) \right) \right]$$
(S4)

1.7   PELDOR Measurement Parameters:

For the Cu^{II}-detected X-band PELDOR measurements, samples of 250 and 220 μM I6R1/K28H/Q32H and I6H/N8H/K28R1 GB1, respectively, were measured either in presence of 1.5 equivalents of Cu^{II}-IDA or Cu^{II}-NTA. The 4-pulse experiment (π/2(υ_A)-τ_1-π(υ_A)-τ_1-t-π(υ_B)-(τ_2-t)-π(υ_A)-τ_2-echo) was used, where υ_A and υ_B indicate the pulse excitation at the observer and pump frequencies, respectively. In all cases monochromatic pulses of lengths 16 and 32 and 12 ns were used for observer and pump pulses (π/2, π and π). The magnetic field and microwave frequency were adjusted to the maximum of the nitroxide spectrum to coincide with the pump pulse position, while the observer pulse spectral position was varied between frequency offsets of 150 and 300 MHz depending on the measurement. Data were acquired with an SRT of 3 ms, a τ_1 of 420 ns and a τ_2 of 1260 ns were used respectively, with 50 shots-per-point and measurements averaged for 12 hours to yield sufficient signal-to-noise ratio (SNR). ^{2}H ESEEM was suppressed using a 16-step t-averaging cycle.

1.8   Modulation Depth Modelling:

The theory section of the main text gives a complete derivation of a multi-site binding polynomial, Z, considered here as a protein with s and t degenerate, non-identical ligand binding sites. It can be shown from multinomial theorem that Z has the form of a double sum for s identical sites with microscopic association constant, K_1, and t identical sites with microscopic association constant, K_2, as shown in equation 11 of the main text. The fractional population of each species is given in equation 8 of the main text. Explicitly, the macroscopic speciation vector, f_i, as it is defined in the main text, is a function of the following parameters: total protein concentration, $[P]_0$, total ligand concentration, $[L]_0$, dissociation constants K_{D1} and K_{D2}, and the numbers of high-affinity and low-affinity sites, s and t, respectively. These fractional macroscopically-bound populations are significant in the simulation of PELDOR modulation depths because each species will contribute to the observed modulation depth with a weighting proportional to the product of their relative population, and the number of spins present in that species, as shown in equation S5:

$$\Delta_{PELDOR} = 1 - \left(\frac{\sum_{i=1}^{N} f_i \times (1 - \lambda_{PELDOR})^{N-1} \times N}{\sum_{i=1}^{N} f_i \times N} \right)$$
(S5)

Where f is as defined in the main text, λ_{PELDOR} is the inversion efficiency of the pumping pulse and N is the total number of spins in the system. The unmodulated echo contributions $(1 - \lambda_{PELDOR})^{N-1}$ are averaged for all species with i = 1 to N ligands bound taking into account the increase in signal and normalising by their contribution to the signal at zero time.[8] PELDOR modulation depths are simulated using Matlab scripts written in-house, and mean square error was used as a metric for simulation quality:

$$mse = mean\left(\left(\Delta_{sim} - \Delta_{exp}\right)^2\right) \tag{S6}$$

1.9   Implementation of Speciation Modelling in Matlab:

The expression of Z as a double sum is rearranged as shown below in equation S7:

$$Z = \sum_{i=0}^{s} \sum_{j=0}^{t} \binom{s}{i}\binom{t}{j} \times (K_1[L])^{s-i}(K_2[L])^{t-j} \tag{S7}$$

To ensure each microscopically-bound species could be easily manipulated in Matlab, it was convenient to separate the binomial coefficients and the variable terms into two block vectors, *C* and *U*. Beginning with the combinatorial coefficients, one can express this product as a block vector, over all *i* permutations of *s* and *j* permutations of *t*, given in equation S8:

$$C = [s_1[t_1 \quad t_2 \quad \dots t_j] \quad s_2[t_1 \quad t_2 \quad \dots t_j] \dots s_i[t_1 \quad t_2 \quad \dots t_j]\,] \tag{S8}$$

This is recognisable as the Kronecker product of two vectors containing the combinatorial coefficients, and preserves the appropriate dimensionality where each coefficient describes the weighting of the associated microscopically-bound state. Similarly, *U* can also be written as a block vector:

$$U = [p_1[q_1 \quad q_2 \quad \dots q_{t+1}] \quad p_2[q_1 \quad q_2 \quad \dots q_{t+1}] \dots p_{s+1}[q_1 \quad q_2 \quad q_{t+1}]\,] \tag{S9}$$

Where for $i = 0 \to s$ and $j = 0 \to t$:

$$p_{i+1} = K_{A1}{}^i[L]^i \tag{S10}$$

$$q_{j+1} = K_{A2}{}^j[L]^j \tag{S11}$$

Therefore, both C and U can be constructed as Kronecker products, and for l-macroscopically bound states, Z can be expressed as a single summation over the microscopic speciation vector *D*:

$$Z = \sum_{i=0}^{l} D_{i+1} \tag{S12}$$

Where:

$$D_i = C_i \times U_i' \tag{S13}$$

And:

$$l = (s + t) + 1 \tag{S14}$$

Let us also consider that one must convert from the microscopic speciation vector D to the macroscopic speciation vector f, because of degeneracy of microscopically-bound species. By reshaping the microscopic speciation vector with dimensions $(s + 1, t + 1)$, this allows indexing of states from unbound to $(s + t)$-bound protein, and can be considered algebraically as:

(s,t)	$t-t$	$t-2$	$t-1$	t
$s-s$	$(t-t)+(s-s)$	$(t-2)+(s-s)$	$(t-1)+(s-s)$	$t+(s-s)$
$s-4$	$(t-t)+(s-4)$	$(t-2)+(s-4)$	$(t-1)+(s-4)$	$t+(s-4)$
$s-3$	$(t-t)+(s-3)$	$(t-2)+(s-3)$	$(t-1)+(s-3)$	$t+(s-3)$
$s-2$	$(t-t)+(s-2)$	$(t-2)+(s-2)$	$(t-1)+(s-2)$	$t+(s-2)$
$s-1$	$(t-t)+(s-1)$	$(t-2)+(s-1)$	$(t-1)+(s-1)$	$t+(s-1)$
s	$(t-t)+s$	$(t-2)+s$	$(t-1)+s$	$t+s$

The transformation from one element to an adjacent anti-diagonal element, if it exists, can be expressed as:

$$D_{i,j} \rightarrow D_{i-1,j+1} \tag{S15}$$

Here, each element in the matrix is related to the total number of ligands bound to the protein molecule, through the summation of its respective coordinates. We also see from this transformation that the sum of coordinates along an anti-diagonal is constant. That is, the total number of ligand molecules bound to the protein molecule is constant along the anti-diagonals, representing degenerate microscopically-bound states that must be summed over to give the appropriate populations of the macroscopically-bound states. This was implemented in Matlab to preclude the need to iteratively expand and solve the polynomial over a triple loop (for values of s, t and $[L]_0$), and remove recursive symbolic substitution steps, to increase computational efficiency. Scripts were tested against numerical calculation to ensure self-consistency, and this approach was found to increase computational efficiency by approximately an order of magnitude.

1.10   Error Propagation For Dissociation Constants Calculated from RIDME Pseudo-titrations:

To provide an error boundary for the estimation of dissociation constants coming from RIDME pseudo-titration series, it was necessary to perform an error analysis. Here, all errors are assumed to be independent, such that all can be approximated by normal distribution functions, and correlation terms between variables are neglected in the subsequent analysis. It should be noted that here we employ two distinct approaches to estimate the error in K_D; i) it can be propagated directly, and ii) it is proportional to the bivariate fitting error, and can be approximated by a fitted Gaussian of the one-dimensional simplex error surface. Let us begin by showing how the error in K_D is propagated directly; since for a system with a single ligand-binding site:

$$\frac{\Delta}{\Delta_{Tmix}} = \frac{(L_0 + P_0 + K_D) - \left(\sqrt{(L_0 + P_0 + K_D)^2 - 4 \times L_0 \times P_0}\right)}{2 \times P_0} \tag{S16}$$

Where: L_0, P_0 and K_D are total concentrations of ligand and protein, and dissociation constant, respectively. While Δ are the experimental modulation depths, and Δ_{Tmix} is as given in the main text (under the mono-exponential approximation of T_1). The expression given for the quotient $\frac{\Delta}{\Delta_{Tmix}}$ can be rearranged as such to yield an expression for K_D:

$$K_D = \frac{\left(\Delta_{Tmix}^2 \times L_0 + \Delta^2 \times P_0 - \Delta \times \Delta_{Tmix} \times L_0 - \Delta \times \Delta_{Tmix} \times P_0\right)}{\Delta \times \Delta_{Tmix}} \tag{S17}$$

Assuming the error in each variable can be accurately approximated, the error in K_D can then be calculated using the variance formula.[9]

While this approach is suitable for error estimation in single measurements, since the K_D is calculated by fitting several measurements, it is perhaps more suitable to approximate the error in K_D using the second approach elaborated above. In this case, the respective errors in Δ and Δ_{Tmix} are assumed to dominate the error in K_D, where the error in Δ is estimated from a statistical distribution of validation trials. The error in Δ_{Tmix} is assumed to be dominated by error in estimating longitudinal relaxation time (T_1) under the mono-exponential approximation. These errors are propagated for the quotient $\frac{\Delta}{\Delta_{Tmix}}$, and K_D is subsequently fitted using a weighted bivariate error function, where the weighting, *w*, is proportional to the reciprocal of the squared error at that point. The weighted error function to be minimised is then given as:

$$rms = \sum \left(w \left(\left(\frac{P_0 + L_0 + K_D - \sqrt{(P_0 + L_0 + K_D)^2 - 4 \times L_0 \times P_0}}{2P_0} \right) - \beta \times \frac{\Delta}{\Delta_{Tmix}} \right)^2 \right) \tag{S18}$$

Where: *w* is the associated weighting of each experimental point, β is the reciprocal scaling factor of Δ_{Tmix} and L_0, P_0, K_D, Δ and Δ_{Tmix} are defined as above. This leads to a weighted 2D error surface, which after finding the optimal reciprocal

scaling factor, reduces to a 1D error surface in K_D. After taking the reciprocal of this weighted root mean square error, this can be approximated as a Gaussian of the form:

$$\frac{1}{rms} = \left(a \times \exp\left(-\left(\frac{(K_D - \mu)}{\sigma} \right)^2 \right) \right) + b \tag{S19}$$

Where: rms is defined as above in equation S18, a is the amplitude of the Gaussian, b is a vertical offset, μ and σ are the mean and standard deviation which define the Gaussian, and K_D is the dissociation constant. The error in K_D is then approximated as σ, and can be calculated within a 95% confidence interval. However, it should be appreciated that this error analysis is only valid for a system containing a single ligand-binding site ($n = 1$).

II   Results and Discussion:

2.1   Inversion Recovery Measurements:

Free and dH-bound Cu^{II}-Chelate T_1 Measurements:

To systematically investigate differences in the longitudinal relaxation behaviours of free- and dH-bound Cu^{II}-chelates, inversion recovery measurements were performed for 1, 10 and 100 µM Cu^{II}-IDA and Cu^{II}-NTA alone, and 1 and 10 µM in presence of 100 µM I6R1/K28H/Q32H GB1, to ensure quantitative double-histidine loading. Raw data and the corresponding fitted mono- and bi-exponential functions are shown in figures S2 and S3 for Cu^{II}-IDA and Cu^{II}-NTA, respectively. Corresponding T_1 estimates and reciprocal e-times are given in tables S1 and S2, respectively. Results are also plotted as an overlay to aide visualisation in figure S4.
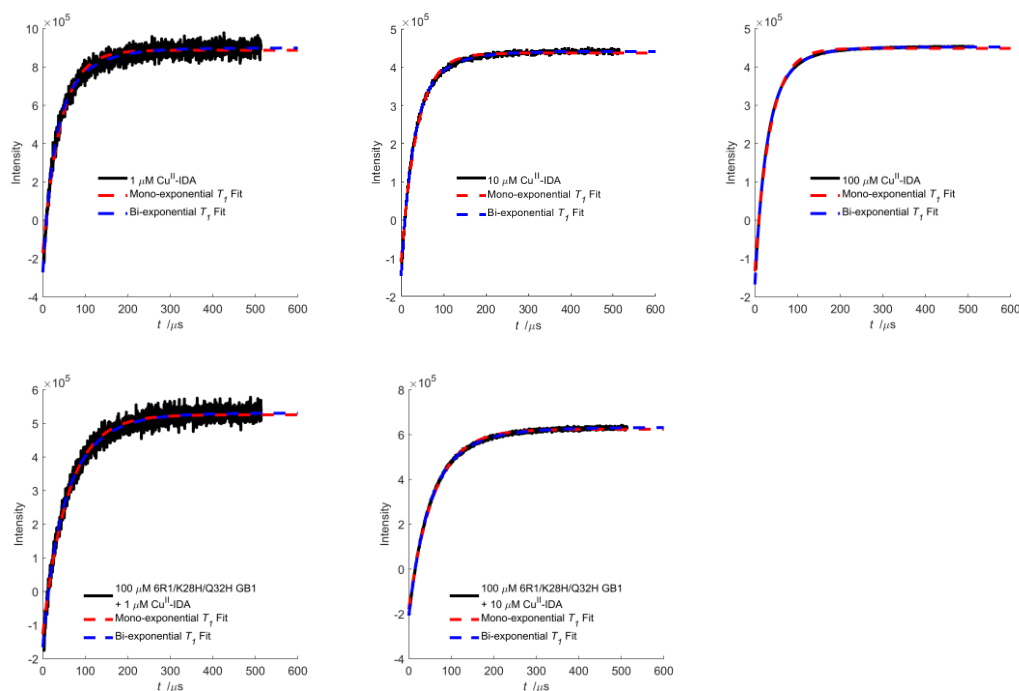

Figure S2. Inversion recovery data for 1, 10 and 100 µM Cu^{II}-IDA (top row), and 1 and 10 µM Cu^{II}-IDA in presence of 100 µM I6R1/K28H/Q32H GB1 shown left-to-right, respectively. The experimental data is shown in black, with the fitted mono-exponential and bi-exponential functions shown as red and blue dotted lines, respectively.
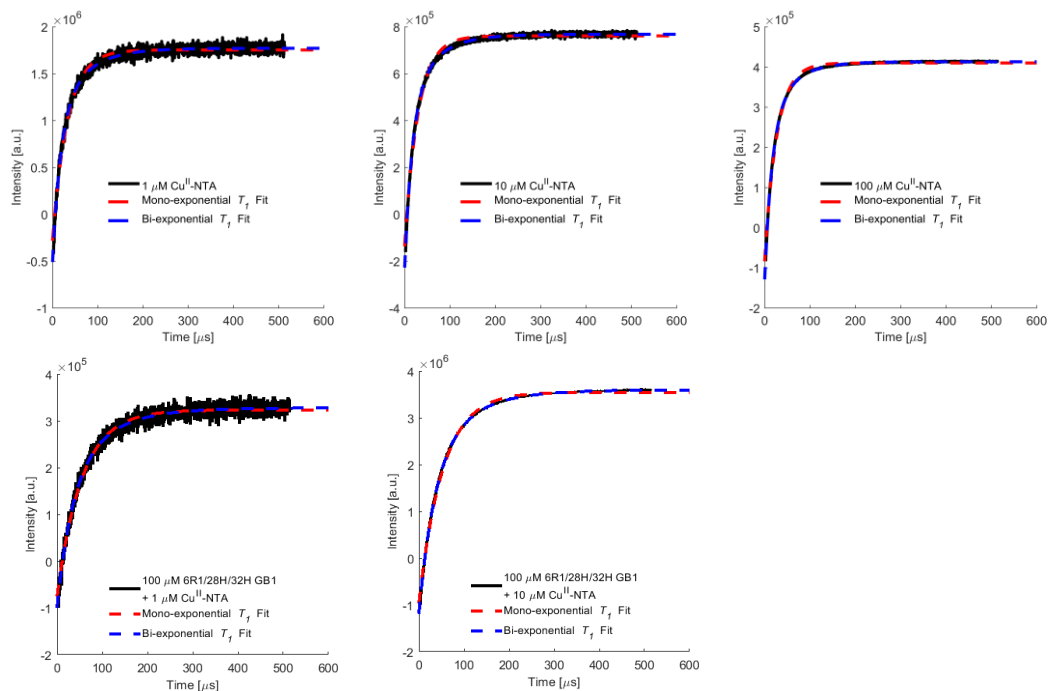
Figure S3. Inversion recovery data for 1, 10 and 100 μM Cu^{II}-NTA (top row), and 1 and 10 μM Cu^{II}-NTA in presence of 100 μM I6R1/K28H/Q32H GB1 shown left-to-right, respectively. The experimental data is shown in black, with the fitted mono-exponential and bi-exponential functions shown as red and blue dotted lines, respectively.
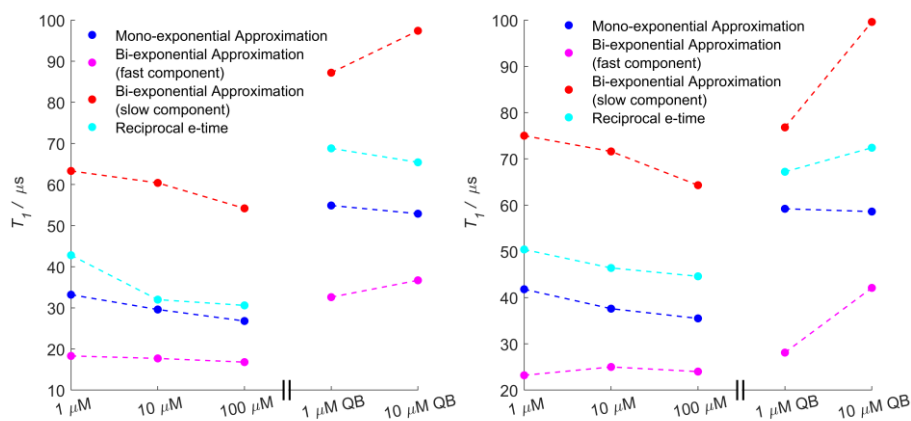

Figure S4. An overlay of the approximations of T_1 from the inversion recovery data shown in figures S2 and S3, for the Cu^{II}-NTA and Cu^{II}-IDA series in the left and right panels respectively. QB indicates the Cu^{II}-chelate is quantitatively double-histidine bound.

Sample	Mono-exponential T_1 [μs]	Bi-exponential T_1 [μs]	1/e time [μs]	$0.5 \times (1/e)^2$ time [μs]
1.0 μM Cu^{II}-IDA	41.8	23.2 (0.62) / 75.0 (0.38)	50.4	55.2
10 μM Cu^{II}-IDA	37.6	25.0 (0.70) / 71.6 (0.30)	46.4	44.6
100 μM Cu^{II}-IDA	35.5	24.0 (0.69) / 64.3 (0.31)	44.6	43.8
100 μM I6R1/K28H/Q32H + 1.0 μM Cu^{II}-IDA	59.2	28.1 (0.36) / 76.8 (0.64)	67.2	61.2
100 μM I6R1/K28H/Q32H + 10 μM Cu^{II}-IDA	58.6	42.1 (0.67) / 99.6 (0.33)	72.4	69.7

Table S1. Mono- and bi-exponential T_1 estimates, and 1/e time for each sample of the series shown in figure S2.

Sample	Mono-exponential T_1 [µs]	Bi-exponential T_1 [µs]	1/e time [µs]	$0.5 \times (1/e)^2$ time [µs]
1.0 µM Cu^{II}-NTA	33.2	18.3 (0.65) / 63.3 (0.35)	42.8	42.7
10 µM Cu^{II}-NTA	29.6	17.7 (0.70) / 60.4 (0.30)	32.0	34.3
100 µM Cu^{II}-NTA	26.8	16.8 (0.72) / 54.2 (0.28)	30.6	32.0
100 µM I6R1/K28H/Q32H + 1.0 µM Cu^{II}-NTA	54.9	32.6 (0.56) / 87.2 (0.44)	68.8	66.6
100 µM I6R1/K28H/Q32H + 10 µM Cu^{II}-NTA	52.9	36.7 (0.68) / 97.4 (0.32)	65.4	65.8

Table S2. Mono- and bi-exponential T_1 estimates, and 1/e time for each sample of the series shown in figure S3.

It can be seen, for both chelates the longitudinal relaxation time of the bound Cu^{II}-chelate is slower than the free component. At temperatures below 50 K diffusion processes and librational motion freeze out, however a free Cu^{II}-chelate interacting with the solvent lattice may experience a greater degree of vibrational perturbation, perhaps through breaking and reformation of co-ordinating hydrogen-bonds. A lattice in which thermal and vibrational motion is minimised leads to a reduced lattice-field, and should in principle give a longer T_1. Even at reasonably low concentrations of 10 µM Cu^{II}-chelate, upon quantitative dH-motif loading, the T_1 approximately doubles. Perhaps this phenomenon is attributable to a different composition of the surrounding lattice at the protein-solvent interface, compared to bulk solvent. Furthermore, the deviations of empirical T_1 values from the mono-exponential approximation were quantified by the deviation from the 1/e time by half of the $(1/e)^2$ time. If the experimental data is perfectly mono-exponential, both values should be identical. It is seen from tables S1 and S2, the mono-exponential condition is largely fulfilled for most cases.

5-pulse Cu^{II}-Cu^{II} RIDME Pseudo-titration T_1 Measurements:

To quantify the modulation depth quotients for the Cu^{II}-Cu^{II} RIDME pseudo-titration series, inversion recovery measurements were performed for 100 µM I6H/N8H/K28H/Q32H GB1 in presence of 50, 70, 100, 170, 500 and 1000 µM Cu^{II}-NTA. Raw data and the corresponding fitted mono- and bi-exponential functions are shown below in figure S5. Corresponding T_1 estimates and reciprocal e-times are given overleaf in table S3.
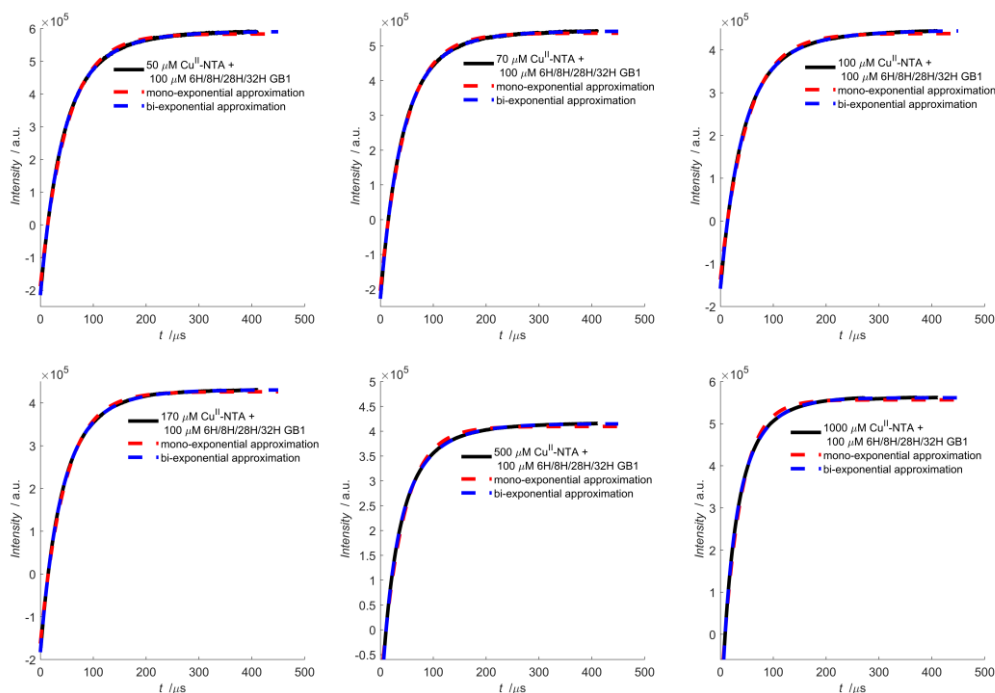

Figure S5 Inversion recovery data for 50, 70, 100 µM Cu^{II}-NTA (top row) and 170, 500 and 1000 µM Cu^{II}-NTA (bottom row), in presence of 100 µM I6H/N8H/K28H/Q32H GB1 shown left-to-right, respectively. The experimental data is shown in black, with the fitted mono-exponential and bi-exponential functions shown as red and blue dotted lines, respectively.

Sample	Mono-exponential T_1 [µs]	Bi-exponential T_1 [µs]	1/e time [µs]	$0.5 \times (1/e)^2$ time [µs]
100 µM 6H/8H/28H/32H + 50 µM Cu^{II}-NTA	49.8 ± 0.16	33.6 (0.57) / 76.7 (0.43)	63.6	60.1
100 µM 6H/8H/28H/32H + 70 µM Cu^{II}-NTA	47.1 ± 0.14	33.4 (0.61) / 72.5 (0.39)	62.8	59.2
100 µM 6H/8H/28H/32H + 100 µM Cu^{II}-NTA	49.7 ± 0.18	34.5 (0.64) / 84.2 (0.36)	63.6	61.5
100 µM 6H/8H/28H/32H + 170 µM Cu^{II}-NTA	46.2 ± 0.14	31.0 (0.55) / 67.8 (0.45)	61.0	59.3
100 µM 6H/8H/28H/32H + 500 µM Cu^{II}-NTA	41.0 ± 0.21	22.8 (0.53) / 64.2 (0.47)	51.8	52.0
100 µM 6H/8H/28H/32H + 1000 µM Cu^{II}-NTA	34.1 ± 0.18	17.5 (0.49) / 50.2 (0.51)	42.6	42.9

Table S3. Mono- and bi-exponential T_1 estimates, and 1/e time for each sample of the series shown in figure S5.

2.2   Electron-spin Echo Decay Measurements:

To investigate whether there was a difference in the transverse relaxation times of free Cu^{II}-chelate, and protein-bound Cu^{II}-chelate, two-pulse electron spin echo measurements were performed for 1, 10 and 100 µM Cu^{II}-IDA and Cu^{II}-NTA alone, and 1 and 10 µM in presence of 100 µM I6R1/K28H/Q32H GB1, to again ensure quantitative double-histidine loading. Raw data and fitted stretched exponential functions are shown in figures S6-7 for Cu^{II}-IDA and Cu^{II}-NTA respectively, and estimates of T_m are given in tables S4-5. Results are also plotted as an overlay to aide visualisation in figure S8. As can be seen, free Cu^{II}-chelate has a faster rate of longitudinal relaxation (T_1), and a slower rate of transverse dephasing (T_m) compared to dH-bound Cu^{II}-chelate. The difference in phase memory time can be explained by considering that the dH-bound component has greater connectivity to the protonated protein framework, and thus dephasing through proton-driven spin-diffusion will be more severe. Conversely, free component is surrounded by the deuterated solvent bath, extending the relative lifetime of electron coherence.
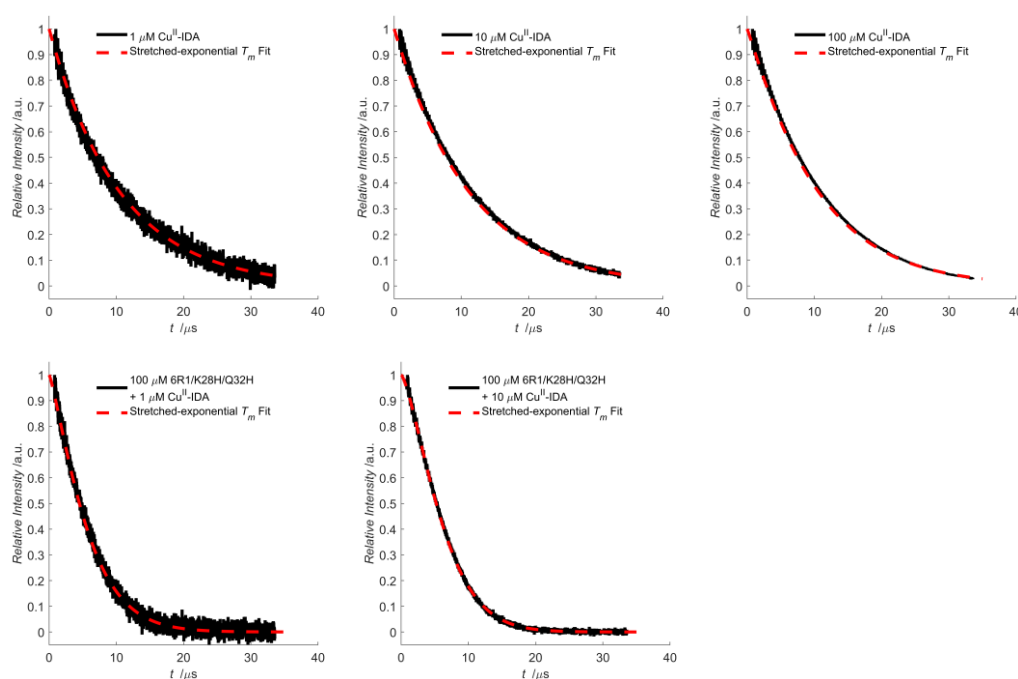

Figure S6. Two-pulse electron spin echo decay data for 1, 10 and 100 µM Cu^{II}-IDA (top row), and 1 and 10 µM Cu^{II}-IDA in presence of 100 µM I6R1/K28H/Q32H GB1 shown left-to-right, respectively. The experimental data is shown in black, with the fitted stretched exponential functions shown as red dotted lines.
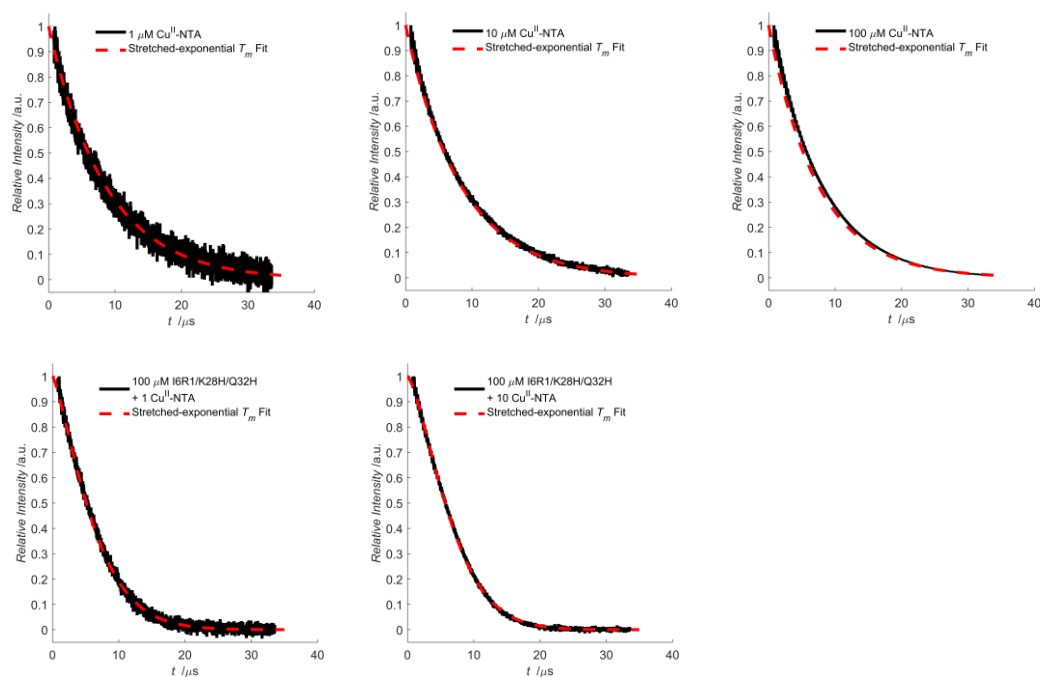
Figure S7. Two-pulse electron spin echo decay data for 1, 10 and 100 µM Cu^{II}-NTA (top row), and 1 and 10 µM Cu^{II}-NTA in presence of 100 µM I6R1/K28H/Q32H GB1 shown left-to-right, respectively. The experimental data is shown in black, with the fitted stretched exponential functions shown as red dotted lines.
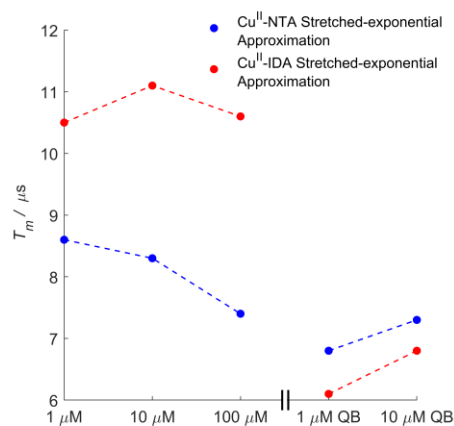

Figure S8. An overlay of the approximations of T_m from the 2-pulse electron spin-echo data shown in figures S6 and S7. The Cu^{II}-NTA and Cu^{II}-IDA series are shown in blue and red, respectively. QB indicates the Cu^{II}-chelate is quantitatively double-histidine bound.

Sample	T_m Estimate [µs]	Stretch Exponent	1/e time [µs]	$0.5 \times (1/e)^2$ time [µs]
1.0 µM Cu^{II}-IDA	10.5	1.00	11.6	11.4
10 µM Cu^{II}-IDA	11.1	1.02	11.8	11.1
100 µM Cu^{II}-IDA	10.6	1.07	11.0	10.4
100 µM I6R1/K28H/Q32H + 1.0 µM Cu^{II}-IDA	6.1	1.23	6.6	5.6
100 µM I6R1/K28H/Q32H + 10 µM Cu^{II}-IDA	6.8	1.41	7.1	5.6

Table S4: Stretched exponential T_m estimates for the Cu^{II}-IDA control series shown in figure S6.

Sample	T_m Estimate [μs]	Stretch Exponent	1/e time [μs]	$0.5 \times (1/e)^2$ time [μs]
1.0 μM Cu^{II}-NTA	8.6	1.00	8.2	11.1
10 μM Cu^{II}-NTA	8.3	1.00	8.6	8.7
100 μM Cu^{II}-NTA	7.4	1.00	8.0	7.8
100 μM I6R1/K28H/Q32H + 1.0 μM Cu^{II}-NTA	6.8	1.30	7.1	5.7
100 μM I6R1/K28H/Q32H + 10 μM Cu^{II}-NTA	7.3	1.43	7.5	5.9

Table S5: Stretched exponential T_m estimates for the Cu^{II}-NTA control series shown in figure S7.

2.3   X-band PELDOR:

Cu^{II}-detected X-band PELDOR[2] measurements were performed for both I6R1/K28H/Q32H and I6H/N8H/K28R1 GB1 in presence of 1.5 equivalents of Cu^{II}-IDA and Cu^{II}-NTA. The raw traces, background corrected dipolar evolution functions and corresponding distance distributions are shown in figures S9-12 below. Background correction parameters are given overleaf in table S6. It should be noted that these samples were prepared with less tightly controlled stoichiometries than the subsequent pseudo-titration series, therefore discussion refrains from direct modulation depth quantitation, and is limited to description of the relative effects. Note that for all PELDOR measurements the distance distributions are not scaled for g-values differing from the free-electron.
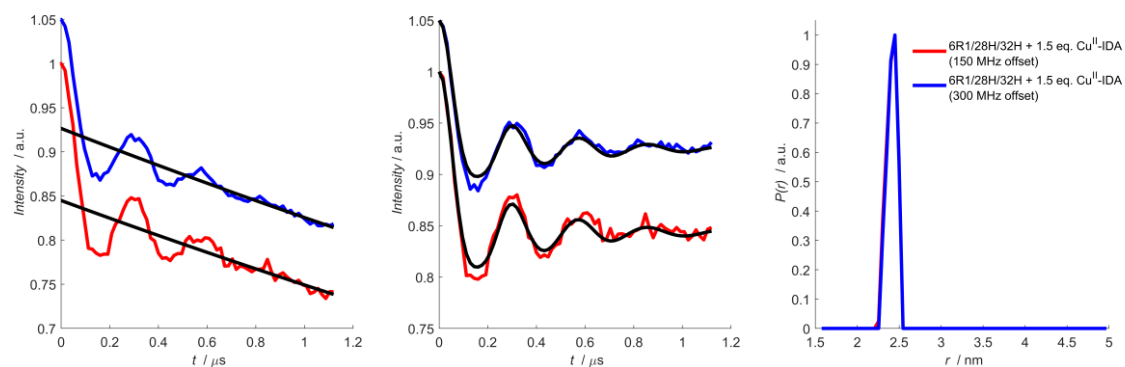

Figure S9: Plot of 6R1/28H/32H GB1 in presence of 1.5 equivalents of Cu^{II}-IDA measured with 150 and 300 MHz frequency offset, are shown as red and blue traces, respectively. The experimental trace, background corrected data, and distance distribution are shown left-to-right respectively.
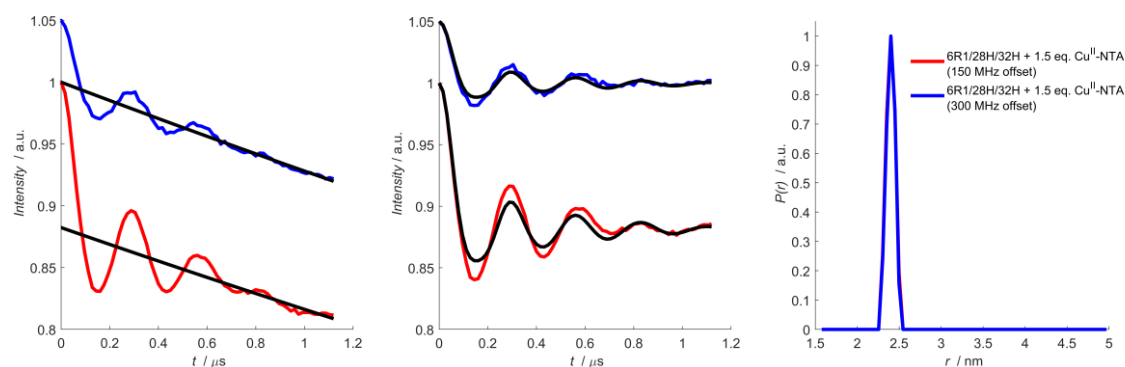

Figure S10: Plot of 6R1/28H/32H GB1 in presence of 1.5 equivalents of Cu^{II}-NTA measured with 150 and 300 MHz frequency offset, are shown as red and blue traces, respectively. The experimental trace, background corrected data, and distance distribution are shown left-to-right respectively.

12

Figure S11: Plot of I6H/N8H/K28R1 GB1 in presence of 1.5 equivalents of Cu^{II}-IDA measured with 150 and 300 MHz frequency offset, are shown as red and blue traces, respectively. The experimental trace, background corrected data, and distance distribution are shown left-to-right respectively.
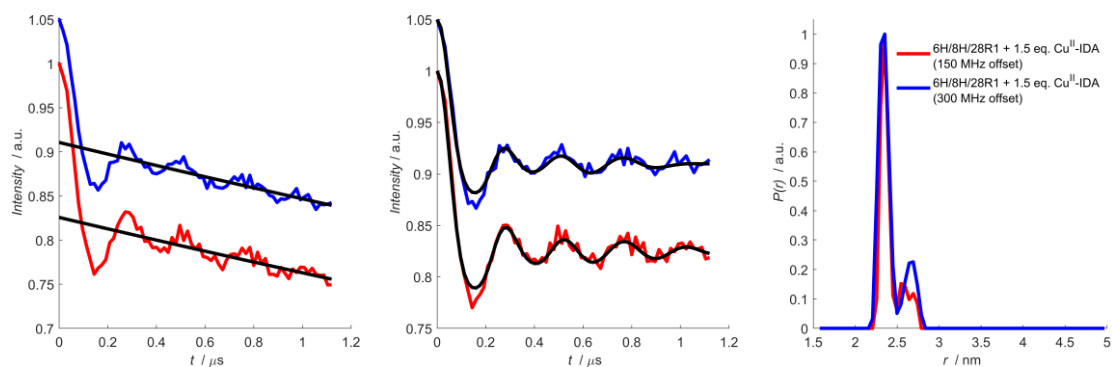

Figure S12: Plot of I6H/N8H/K28R1 GB1 in presence of 1.5 equivalents of Cu^{II}-NTA measured with 150 and 300 MHz frequency offset, are shown as red and blue traces, respectively. The experimental trace, background corrected data, and distance distribution are shown left-to-right respectively.
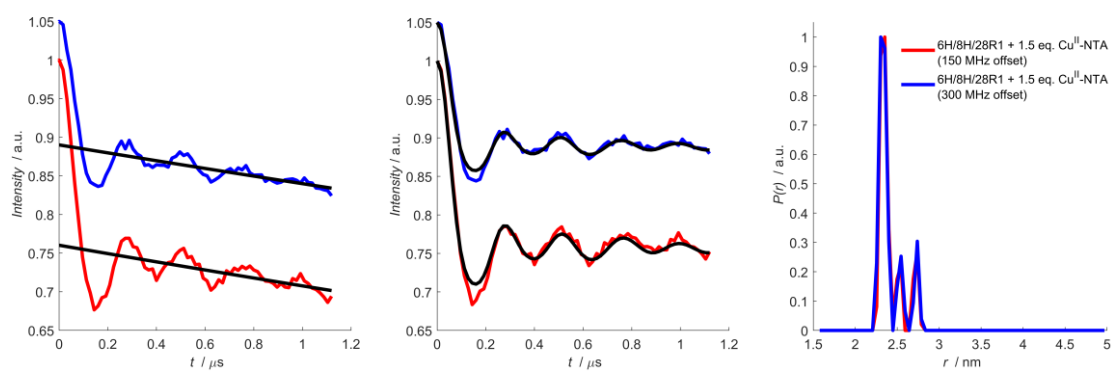
Sample	Zero-time (ns)	Background start (ns)	Background Cut-off (ns)	Δ
6R1/28H/32H GB1 + Cu^{II}-NTA (150 MHz offset)	341	328	1120	0.118
6R1/28H/32H GB1 + Cu^{II}-NTA (300 MHz offset)	341	328	1120	0.050
6R1/28H/32H GB1 + Cu^{II}-IDA (150 MHz offset)	339	328	1120	0.155
6R1/28H/32H GB1 + Cu^{II}-IDA (300 MHz offset)	339	328	1120	0.124
6H/8H/28R1 GB1 + Cu^{II}-NTA (150 MHz offset)	339	328	1120	0.240
6H/8H/28R1 GB1 + Cu^{II}-NTA (300 MHz offset)	340	328	1120	0.160
6H/8H/28R1 GB1 + Cu^{II}-IDA (150 MHz offset)	340	328	1120	0.174
6H/8H/28R1 GB1 + Cu^{II}-IDA (300 MHz offset)	338	328	1120	0.139

Table S6: Comparison of background correction parameters and modulation depths for the PELDOR traces shown in figures S9-12.

Whilst all nitroxides will to good approximation have identical EPR spectra and relaxation behaviour whether they are tethered to a protein with a free or occupied dH site this approximation is not well met for the Cu^{II}-based spins, as demonstrated in sections 2.1 and 2.2 above. This means that in Cu^{II}-detected PDEPR the ratio of free and dH bound Cu^{II} does not only depend on their stoichiometric factors but also the exact position in the EPR spectrum that is detected. This can be seen when recording X-band Cu^{II}-NO PELDOR detecting different regions of the Cu^{II} spectrum. Figures S9-12 demonstrate that detecting the maximum of the Cu^{II} spectrum (at 300 MHz higher frequency than the maximum of the NO spectrum) systematically yields a lower Δ than detecting the high field edge of the Cu^{II} spectrum (at 150 MHz higher frequency than the maximum of the NO spectrum). Previous literature values[10] and simulation of free and dH-bound Cu^{II}-chelate using Easyspin[11] , indicated g$_{II}$ is smaller for the dH-bound, relative to the free component, resulting in greater excitation at lower offset, consistent with the observed trend. This is attributed to a higher spectral intensity of free relative

to dH bound Cu^{II} at the larger offset compared to the smaller offset, confounding quantification from Cu^{II}-detected PDEPR. Easyspin[11] simulations of the free- and dH-bound Cu^{II}-chelate component spectra at Q-band frequency were performed, with results shown overleaf in figure S13 and simulation parameters are given below in table S7.
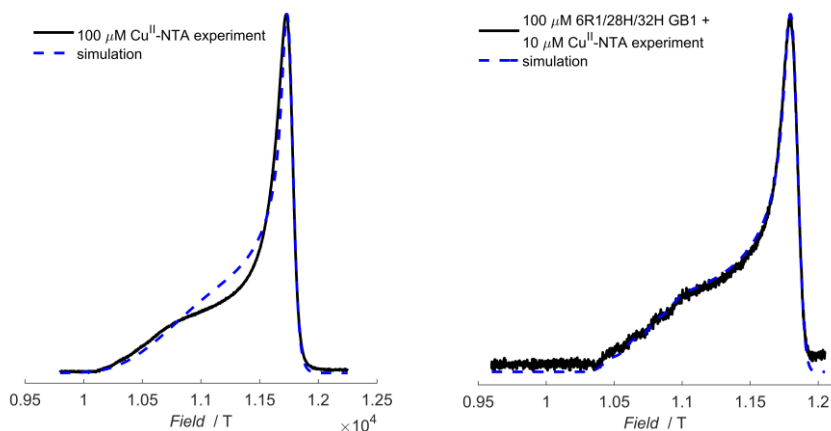

Figure S13: Absorbance spectra (echo-detected field sweep, EDFS) of 100 µM Cu^{II}-NTA (left panel) and 100 µM 6R1/28H/32H GB1 in presence of 10 µM Cu^{II}-NTA chelate (right panel), with experimental and simulated traces in black (solid) and blue (dotted) respectively.

Sample	g⊥	g‖	A‖ [MHz]	A⊥ [MHz]	A‖ strain [MHz]	A⊥ strain [MHz]	H‖ strain [MHz]	H⊥ strain [MHz]	Gaussian Linewidth [mT]	Simulation RMSD [a.u.]
100 µM Cu^{II}-NTA	2.0679	2.2867	27.932	570.00	-	-	20.436	1600	6.7800	3.00 x 10^{-2}
100 µM 6R1/28H/32H + 10 µM Cu^{II}-NTA	2.0216	2.2365	27.934	522.71	93.053	194.44	-	-	8.7129	1.94 x 10^{-2}

Table S7: Parameters of the simulated absorbance spectra shown in figure S13.

It is important to note that while the broad feature at low field in the free Cu^{II}-NTA absorbance spectrum is likely to be underdetermined, for qualitative support of the observed trend in modulation depth, the simulation is sufficient.

2.4   Q-band RIDME:

Cu^{II}-detected Q-band RIDME measurements were performed for 100 µM I6H/N8H/K28H/Q32H GB1 in presence of 50, 70, 100, 170, 500 and 1000 µM Cu^{II}-NTA. The raw traces, background corrected dipolar evolution functions and corresponding distance distributions (where a stretched exponential background function for background correction is used) are shown in figure 2 of the main text. Similarly, the raw traces, background corrected dipolar evolution functions and corresponding distance distributions (where a second-order polynomial background function for background correction is used) are shown below in figures S14-19. Background correction parameters and modulation depths are given in table S8. Only the RIDME series recorded using a T_{mix} and T_1 ratio of 0.7 are shown in this section. For validated Q-band RIDME data recorded using all T_{mix} and T_1 ratios, all background correction models, and further discussion see sections 2.5 and 2.6 below. Note that for all RIDME measurements the distance distributions are not scaled for g-values differing from the free-electron.
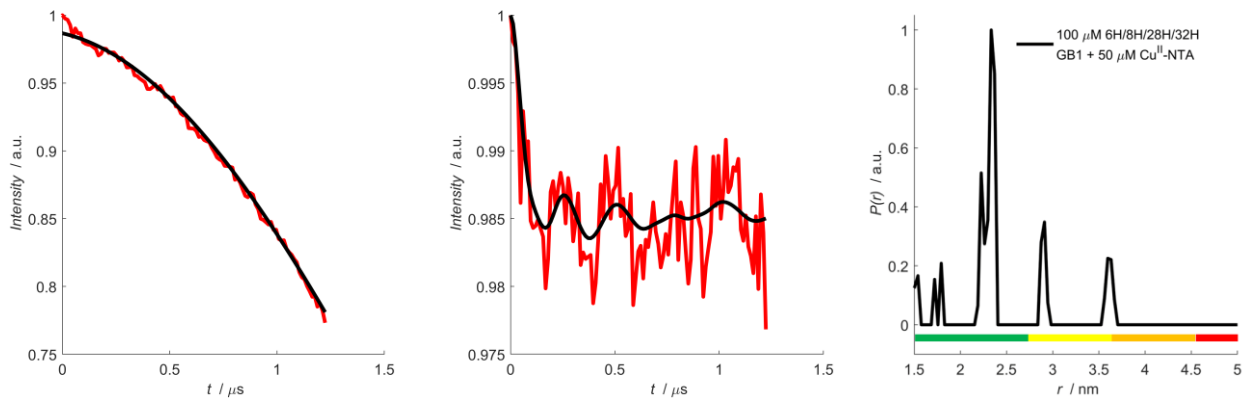
Figure S14: Plot of non-deconvoluted 50 µM Cu^{II}-NTA pseudo-titration data. The experimental trace, background corrected data, and distance distribution, are shown left-to-right respectively. The background correction of the raw data and corresponding fitted dipolar evolution function are shown in black.

Figure S15: Plot of non-deconvoluted 70 µM Cu^{II}-NTA pseudo-titration data. The experimental trace, background corrected data, and distance distribution, are shown left-to-right respectively. The background correction of the raw data and corresponding fitted dipolar evolution function are shown in black. The asterisk indicates the position of a standing echo artefact.
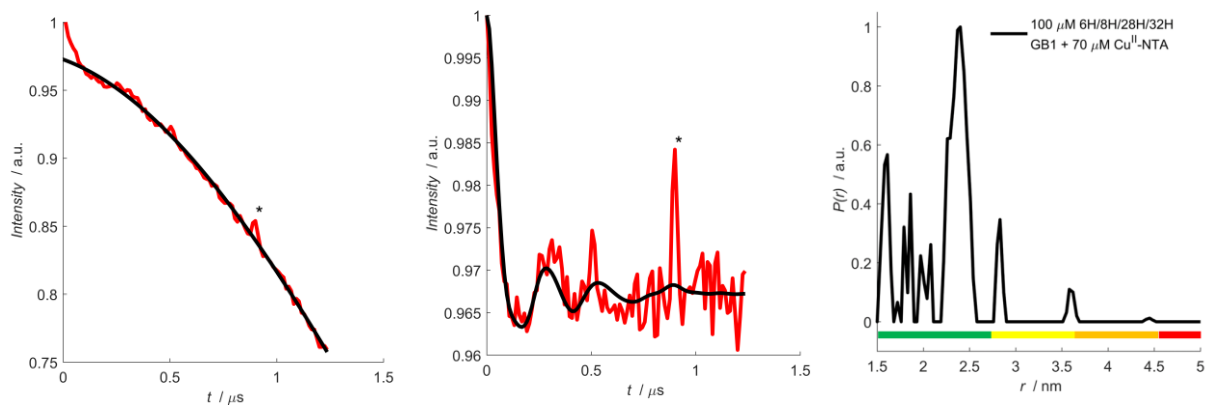

Figure S16: Plot of non-deconvoluted 100 µM Cu^{II}-NTA pseudo-titration data. The experimental trace, background corrected data, and distance distribution, are shown left-to-right respectively. The background correction of the raw data and corresponding fitted dipolar evolution function are shown in black. The asterisk indicates the position of a standing echo artefact.
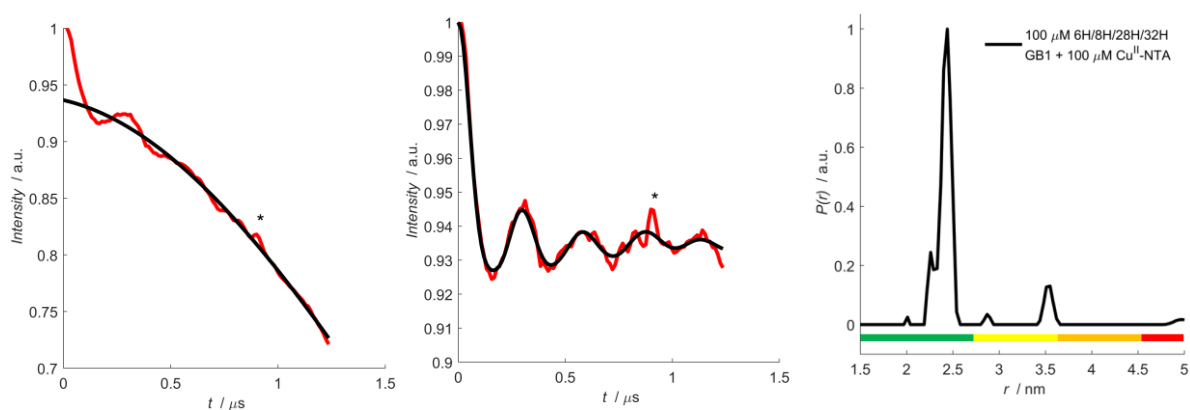
Figure S17: Plot of non-deconvoluted 170 µM Cu^{II}-NTA pseudo-titration data. The experimental trace, background corrected data, and distance distribution, are shown left-to-right respectively. The background correction of the raw data and corresponding fitted dipolar evolution function are shown in black. The asterisk indicates the position of a standing echo artefact.
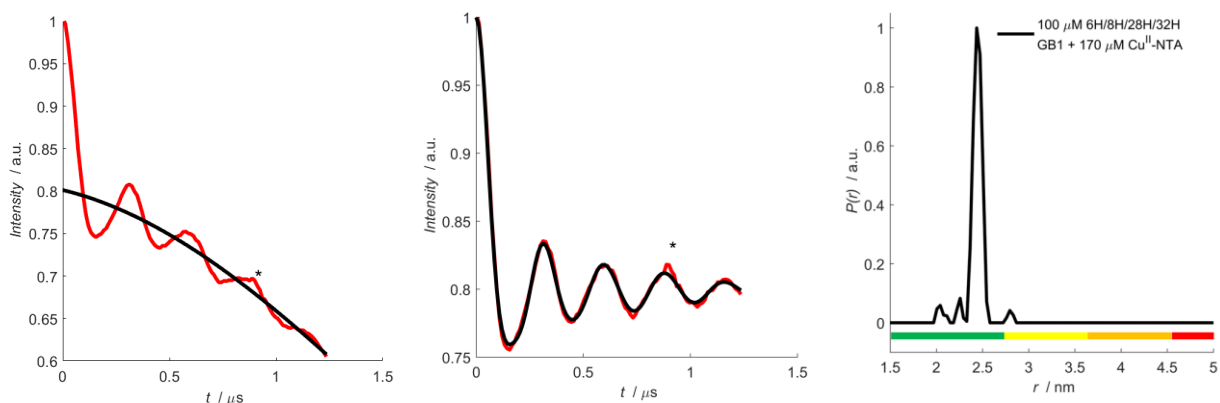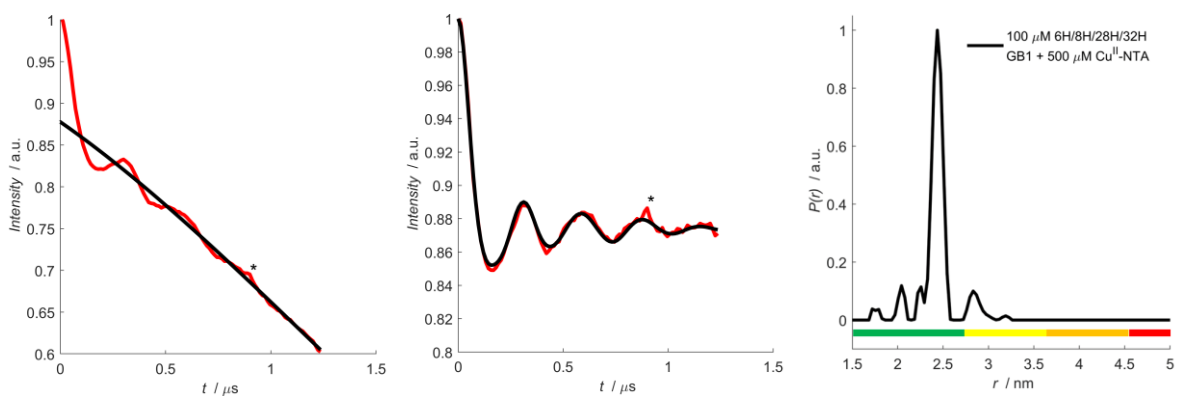

Figure S18: Plot of non-deconvoluted 500 µM Cu^{II}-NTA pseudo-titration data. The experimental trace, background corrected data, and distance distribution, are shown left-to-right respectively. The background correction of the raw data and corresponding fitted dipolar evolution function are shown in black. The asterisk indicates the position of a standing echo artefact.
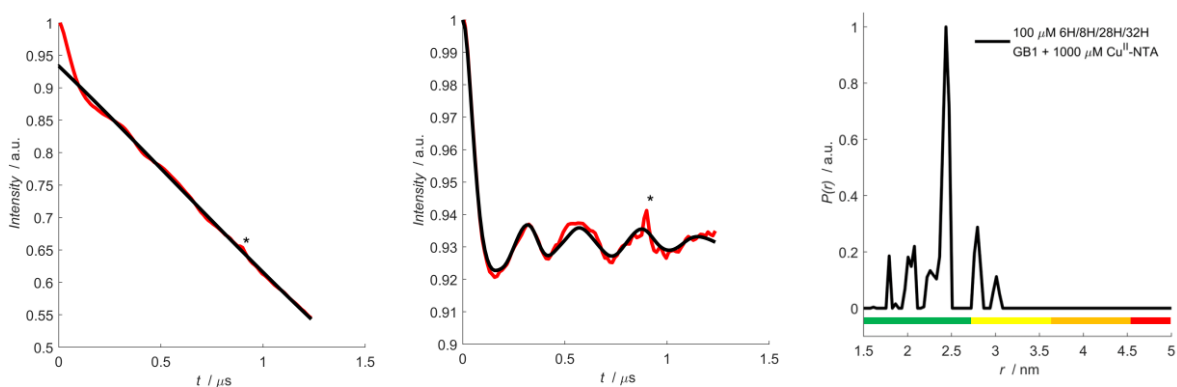
Figure S19: Plot of non-deconvoluted 1000 µM Cu^{II}-NTA pseudo-titration data. The experimental trace, background corrected data, and distance distribution, are shown left-to-right respectively. The background correction of the raw data and corresponding fitted dipolar evolution function are shown in black. The asterisk indicates the position of a standing echo artefact.

16

Sample	Zero-time (ns)	Background start (ns)	Background Cut-off (ns)	Δ
100 µM 6H/8H/28H/32H GB1 + 50 µM Cu-NTA	219	108	1224	0.013
100 µM 6H/8H/28H/32H GB1 + 70 µM Cu-NTA	211	168	1236	0.027
100 µM 6H/8H/28H/32H GB1 + 100 µM Cu-NTA	211	309	1236	0.063
100 µM 6H/8H/28H/32H GB1 + 170 µM Cu-NTA	208	192	1236	0.199
100 µM 6H/8H/28H/32H GB1 + 500 µM Cu-NTA	208	309	1236	0.122
100 µM 6H/8H/28H/32H GB1 + 1000 µM Cu-NTA	210	216	1236	0.066

Table S8: Comparison of background correction parameters and modulation depths for the RIDME traces shown in figures S14-19.

2.5   Cu^{II}-Nitroxide RIDME Pseudo-Titration Validations:

To estimate the error in RIDME modulation depths as a function of background correction parameters and noise level, it was necessary to assess the utility of the validation tool in DeerAnalysis2018[6] when applied to RIDME traces, to check the Tikhonov validation of the corresponding distance distributions. For completion, the deconvoluted experimental traces, background corrected traces, validated distance distributions, and a histogram representation of the distribution of modulation depths for the validation run are shown in figures S20-24, respectively. For each histogram, a normal distribution is overlaid, and is calculated using:

$$f(x) = \frac{1}{\sqrt{2\pi\sigma^2}} exp\left(-\frac{(x-\mu)^2}{2\sigma^2}\right) \qquad (S20)$$

where: μ and σ are the mean and standard deviation which define the Gaussian, and x is the modulation depth calculated for each Tikhonov validation trial.

Figure S20: Plot of deconvoluted 100 nM Cu^{II}-NTA pseudo-titration data. The deconvoluted experimental trace, background corrected data, the validated distance distribution, and a histogram showing the distribution of Δ for trials within a 1.15 prune level, are shown left-to-right respectively. The mean of the distance distribution is shown as the black trace, with the 2σ confidence interval shown as the shaded region.
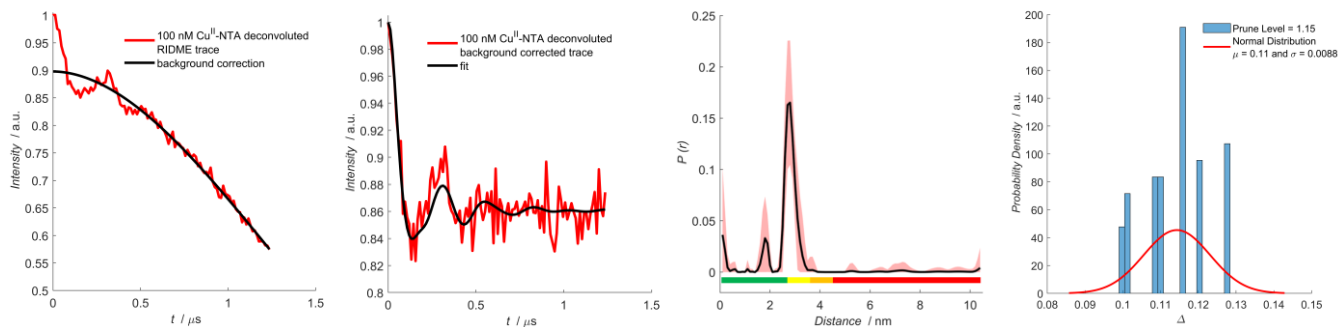

Figure S21: Plot of deconvoluted 300 nM Cu^{II}-NTA pseudo-titration data. The deconvoluted experimental trace, background corrected data, the validated distance distribution, and a histogram showing the distribution of Δ for trials within a 1.15 prune level are shown left-to-right respectively. The mean of the distance distribution is shown as the black trace, with the 2σ confidence interval shown as the shaded region.

Figure S22: Plot of deconvoluted 900 nM Cu^{II}-NTA pseudo-titration data. The deconvoluted experimental trace, background corrected data, the validated distance distribution, and a histogram showing the distribution of Δ for trials within a 1.15 prune level, are shown left-to-right respectively. The mean of the distance distribution is shown as the black trace, with the 2σ confidence interval shown as the shaded region.
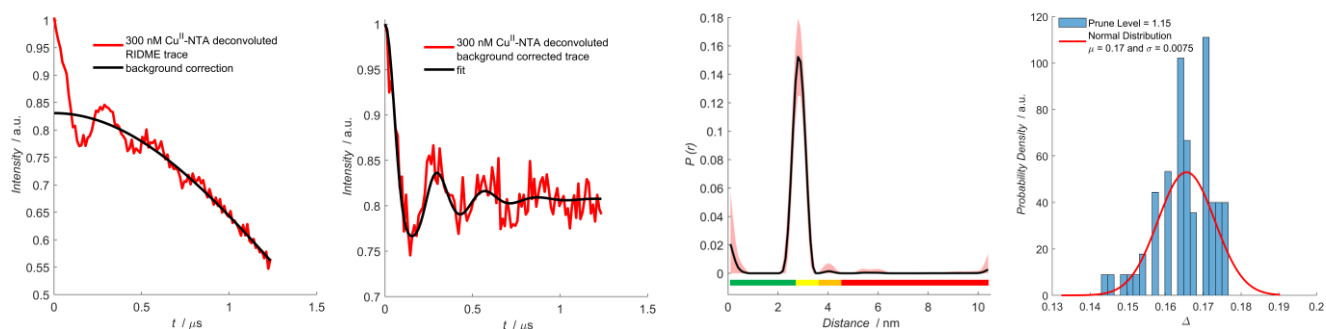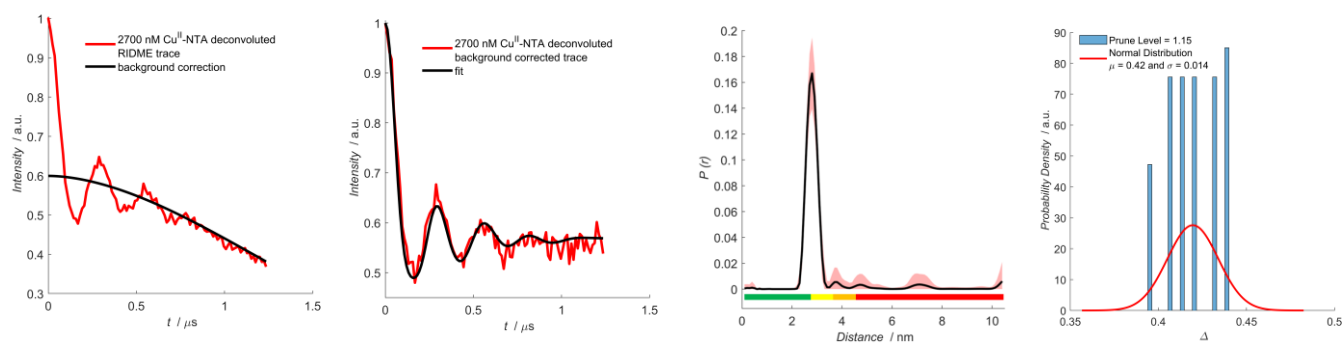
Figure S23: Plot of deconvoluted 2700 nM Cu^{II}-NTA pseudo-titration data. The deconvoluted experimental trace, background corrected data, the validated distance distribution, and a histogram showing the distribution of Δ for trials within a 1.15 prune level, are shown left-to-right respectively. The mean of the distance distribution is shown as the black trace, with the 2σ confidence interval shown as the shaded region.
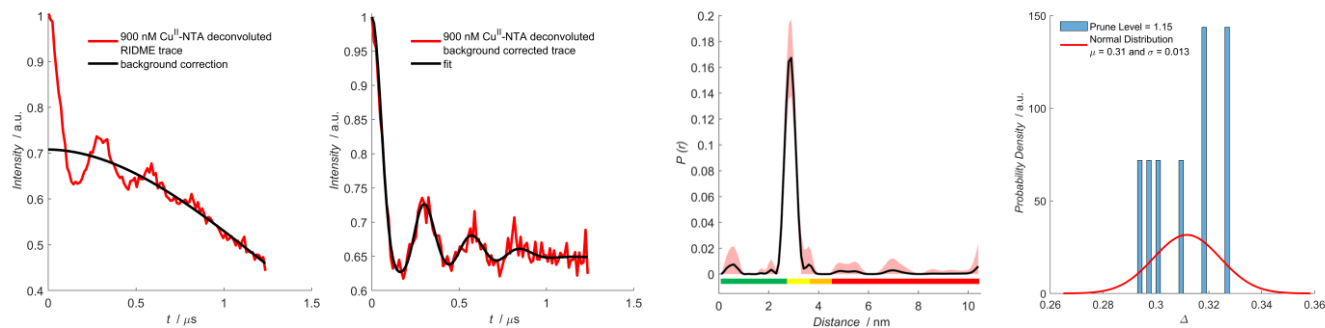

Figure S24: Plot of deconvoluted 8100 nM Cu^{II}-NTA pseudo-titration data. The deconvoluted experimental trace, background corrected data, the validated distance distribution, and a histogram showing the distribution of Δ for trials within a 1.15 prune level, are shown left-to-right respectively. The mean of the distance distribution is shown as the black trace, with the 2σ confidence interval shown as the shaded region.
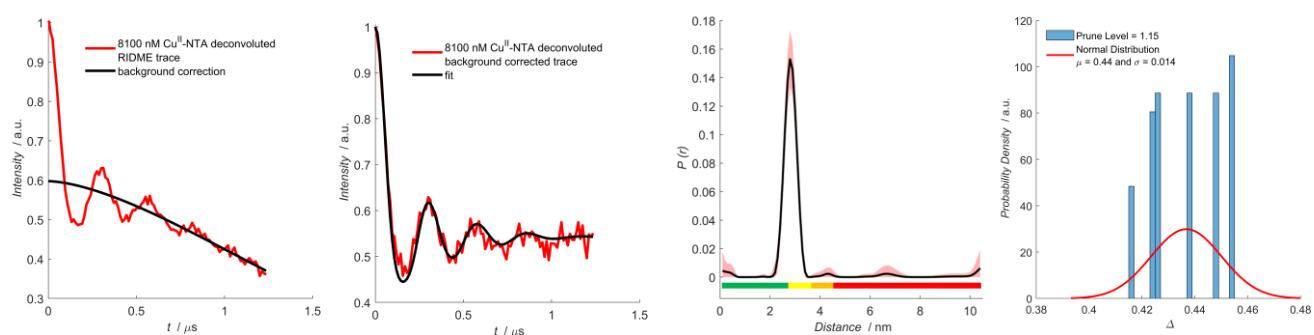
Background correction parameters and modulation depths for each sample are given below in table S9.

Sample	Zero-time (ns)	Background start (ns)	Background Cut-off (ns)	Δ	Background Dimension
100 nM Cu-NTA	207	150	1232	0.102	3.0
300 nM Cu-NTA	206	239	1232	0.169	6.0
900 nM Cu-NTA	206	371	1232	0.292	3.0
2700 nM Cu-NTA	207	62	1232	0.400	3.0
8100 nM Cu-NTA	205	238	1232	0.402	3.0

Table S9: Comparison of background correction parameters for the deconvoluted RIDME traces shown in figures S20-24.

For all deconvoluted RIDME traces, the validated distance distributions show that only the main peak observed at 2.5 nm is significant, since at all other distances, the lower estimate (shown in the unfilled space) has a probability density of 0 and therefore is within the noise floor. This is also encouraging that regardless of background correction parameter choice, the distance distribution is preserved, however the observed modulation depth is generally more sensitive to the choice of background correction parameters. Even so, all modulation depths carried forward for additional processing were found to be within ± 2 σ of the distribution mean. It is seen that all modulation depth distributions have 95% confidence intervals within ± 0.03 of the distribution mean. It should also be noted that because deconvolution suppresses the low frequency artefact, trials in which the root mean square deviation is dominated by this feature are minimised.

2.6   *Cu^{II}-Cu^{II} RIDME Pseudo-Titration Validations:*

Stretched Exponential Background Correction:

Figure S25: Plot of non-deconvoluted 50 µM Cu^{II}-NTA pseudo-titration data performed with 35 (top row) and 95 (bottom row) µs mixing times. The non-deconvoluted experimental trace, background corrected data, and the validated distance distribution, are shown left-to-right respectively. The mean of the distance distribution is shown as the black trace, with the 2σ confidence interval shown as the shaded region.

Figure S26: Plot of non-deconvoluted 70 μM Cu[II]-NTA pseudo-titration data performed with 33 (top row), 61 (middle row) and 89 (bottom row) μs mixing times. The non-deconvoluted experimental trace, background corrected data, and the validated distance distribution, are shown left-to-right respectively. The mean of the distance distribution is shown as the black trace, with the 2σ confidence interval shown as the shaded region.
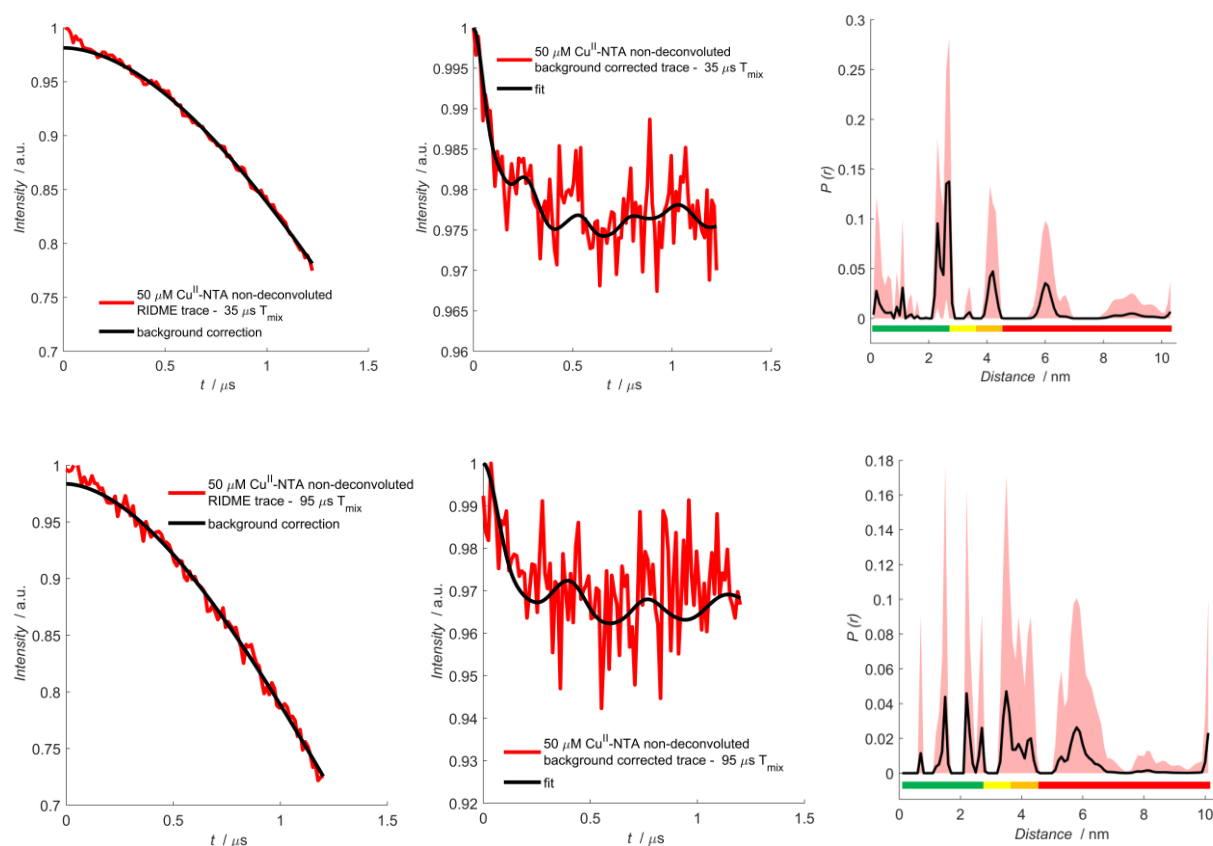
Figure S27: Plot of non-deconvoluted 100 μM Cu^{II}-NTA pseudo-titration data performed with 35 (top row), 65 (middle row) and 95 (bottom row) μs mixing times. The non-deconvoluted experimental trace, background corrected data, and the validated distance distribution, are shown left-to-right respectively. The mean of the distance distribution is shown as the black trace, with the 2σ confidence interval shown as the shaded region.
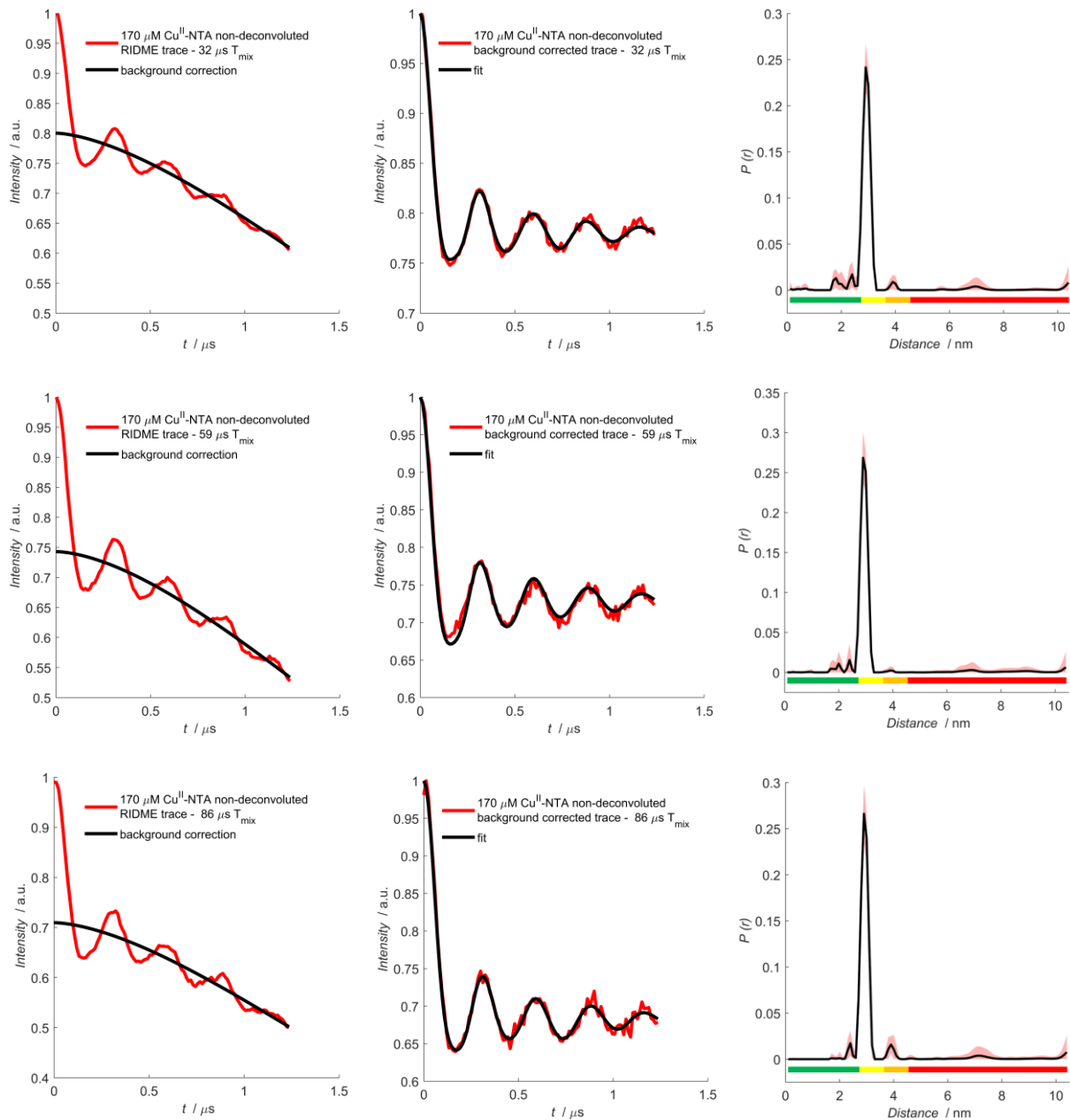
Figure S28: Plot of non-deconvoluted 170 μM Cu^{II}-NTA pseudo-titration data performed with 32 (top row), 59 (middle row) and 86 (bottom row) μs mixing times. The non-deconvoluted experimental trace, background corrected data, and the validated distance distribution, are shown left-to-right respectively. The mean of the distance distribution is shown as the black trace, with the 2σ confidence interval shown as the shaded region.
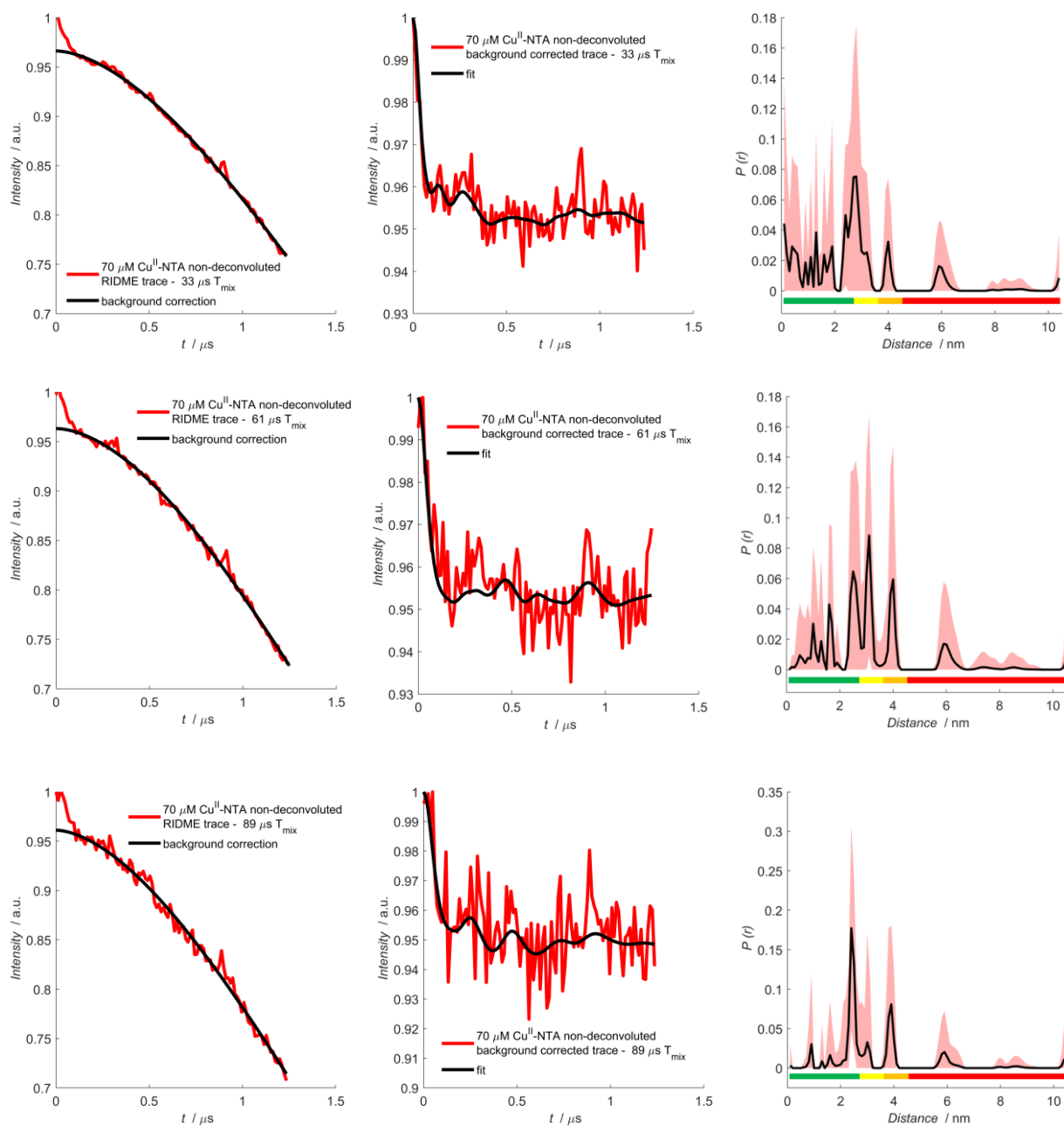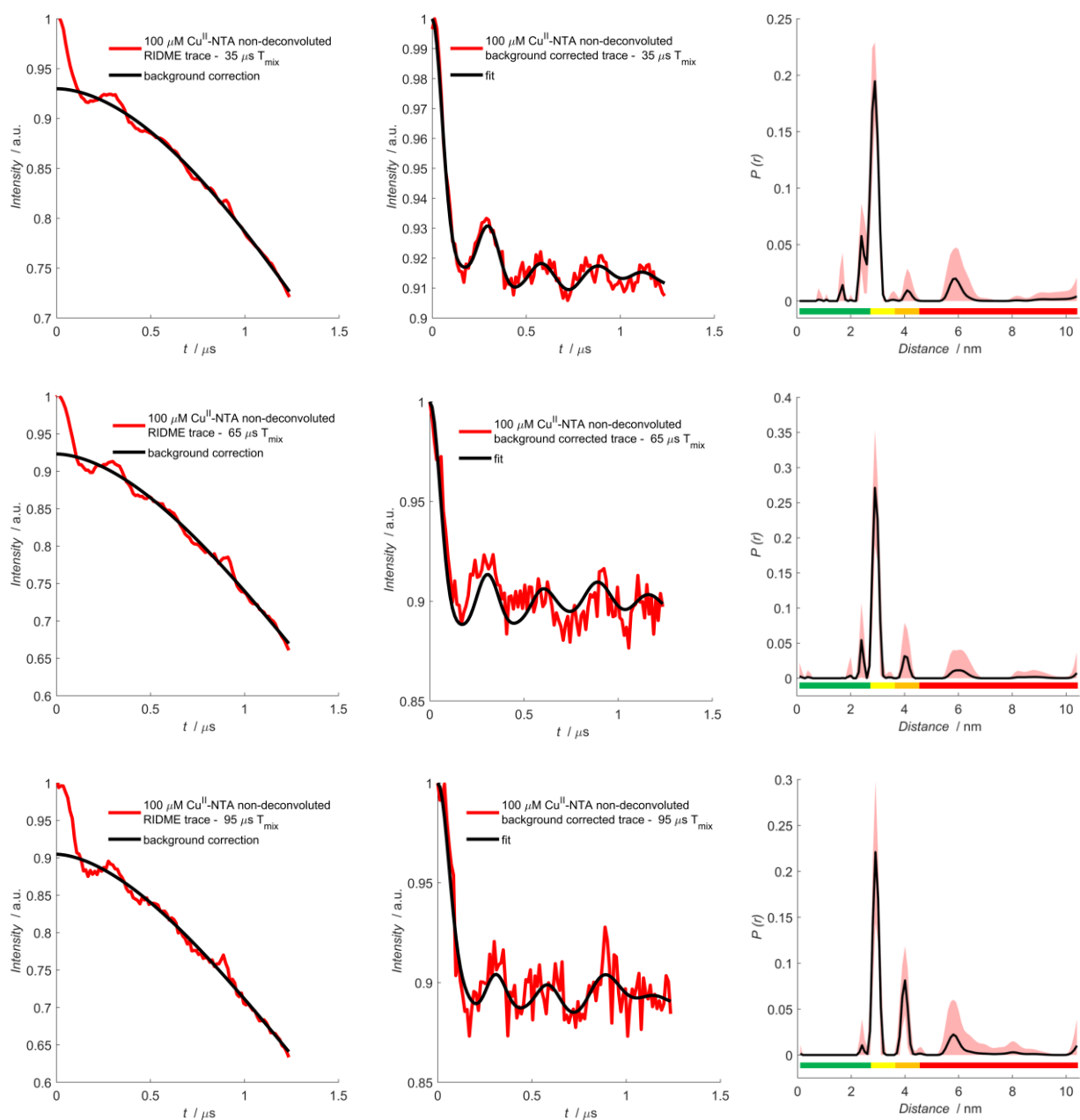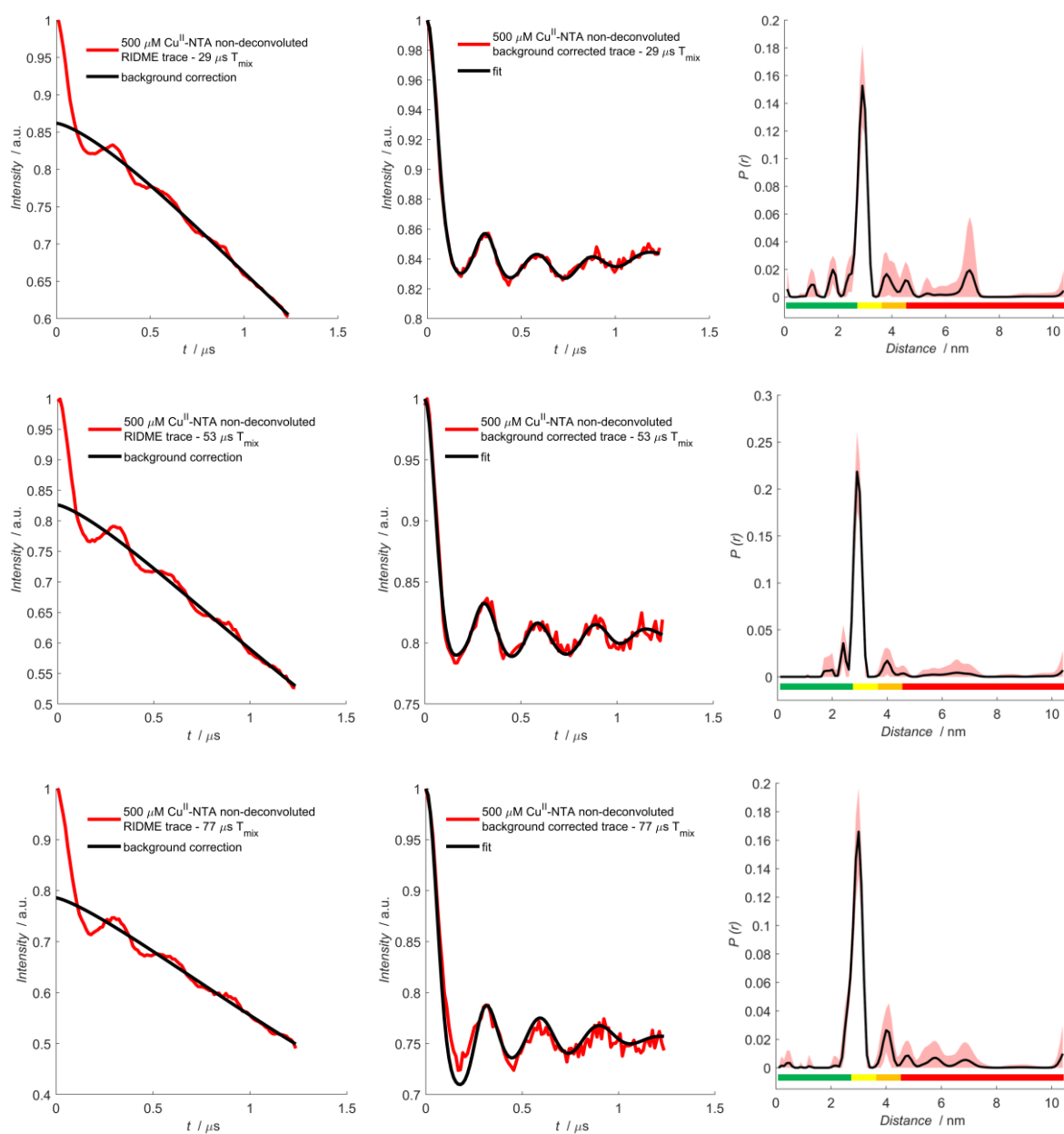
Figure S29: Plot of non-deconvoluted 500 μM Cu^{II}-NTA pseudo-titration data performed with 29 (top row), 53 (middle row) and 77 (bottom row) μs mixing times. The non-deconvoluted experimental trace, background corrected data, and the validated distance distribution, are shown left-to-right respectively. The mean of the distance distribution is shown as the black trace, with the 2σ confidence interval shown as the shaded region.

Figure S30: Plot of non-deconvoluted 1000 μM Cu^II-NTA pseudo-titration data performed with 24 (top row), 43 (middle row) and 62 (bottom row) μs mixing times. The non-deconvoluted experimental trace, background corrected data, and the validated distance distribution, are shown left-to-right respectively. The mean of the distance distribution is shown as the black trace, with the 2σ confidence interval shown as the shaded region.
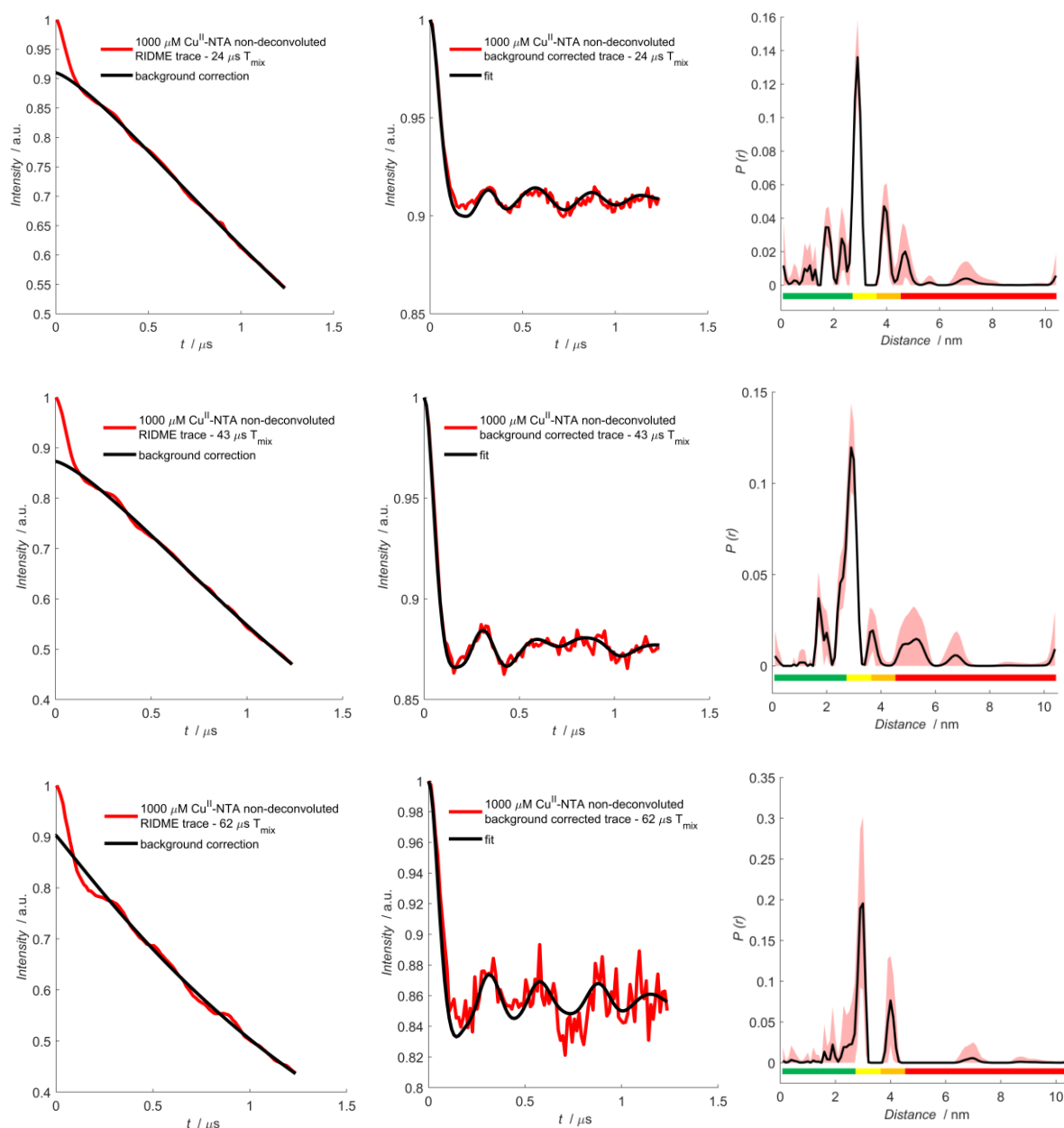
Background correction parameters and modulation depths for each sample are given overleaf in table S10.

Sample	Mixing time [µs]			Zero-time [ns]			Background Start [ns]			Background Cut-off [ns]			Δ		
100 µM 6H/8H/28H/32H + 50 µM Cu^{II}-NTA	35	65	95	219	-	241	328	-	239	1224	-	1200	0.019 ± 4.6 x 10^{-3}	-	0.016 ± 5.8 x 10^{-3}
100 µM 6H/8H/28H/32H + 70 µM Cu^{II}-NTA	33	61	89	211	203	213	372	372	328	1236	1248	1236	0.034 ± 5.0 x 10^{-3}	0.037 ± 5.6 x 10^{-3}	0.039 ± 6.4 x 10^{-3}
100 µM 6H/8H/28H/32H + 100 µM Cu^{II}-NTA	35	65	95	211	210	216	372	284	106	1236	1236	1236	0.070 ± 1.1 x 10^{-2}	0.077 ± 1.5 x 10^{-2}	0.095 ± 1.8 x 10^{-2}
100 µM 6H/8H/28H/32H + 170 µM Cu^{II}-NTA	32	59	86	208	207	208	372	328	106	1236	1236	1236	0.200 ± 1.5 x 10^{-2}	0.257 ± 2.2 x 10^{-2}	0.290 ± 2.4 x 10^{-2}
100 µM 6H/8H/28H/32H + 500 µM Cu^{II}-NTA	29	53	77	208	207	208	283	106	283	1236	1236	1236	0.138 ± 1.8 x 10^{-2}	0.174 ± 2.6 x 10^{-2}	0.214 ± 2.6 x 10^{-2}
100 µM 6H/8H/28H/32H + 1000 µM Cu^{II}-NTA	24	43	62	210	208	207	239	239	372	1236	1236	1236	0.090 ± 8.2 x 10^{-3}	0.127 ± 1.2 x 10^{-2}	0.098 ± 2.0 x 10^{-2}

Table S10: Comparison of background correction parameters for the validated non-deconvoluted RIDME traces, using a stretched exponential background function, shown in figures S25-30. The error in modulation depth is ± 2σ.

Second-order Polynomial Background Correction:

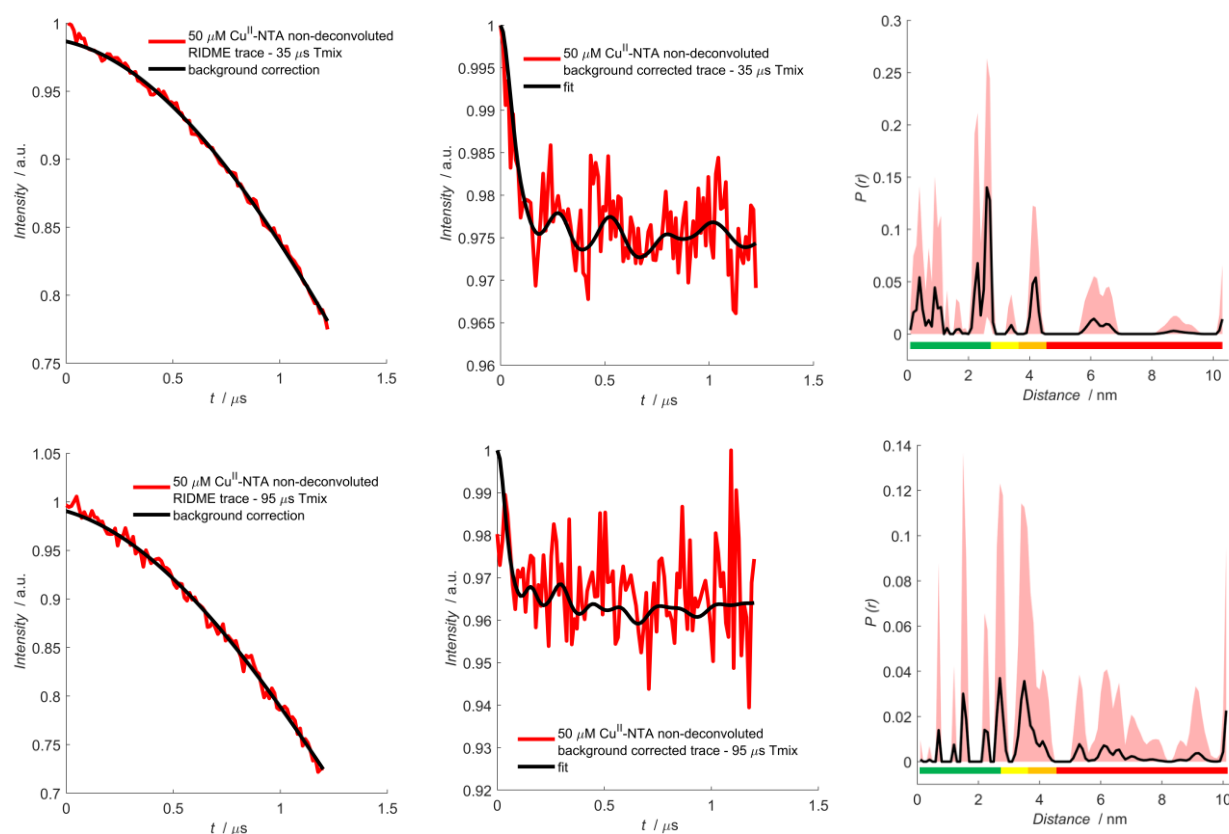**Figure S31**: Plot of non-deconvoluted 50 µM Cu^{II}-NTA pseudo-titration data performed with 35 (top row) and 95 (bottom row) µs mixing times. The non-deconvoluted experimental trace, background corrected data, and the validated distance distribution, are shown left-to-right respectively. The mean of the distance distribution is shown as the black trace, with the 2σ confidence interval shown as the shaded region.

Figure S32: Plot of non-deconvoluted 70 µM Cu^{II}-NTA pseudo-titration data performed with 33 (top row), 61 (middle row) and 89 (bottom row) µs mixing times. The non-deconvoluted experimental trace, background corrected data, and the validated distance distribution, are shown left-to-right respectively. The mean of the distance distribution is shown as the black trace, with the 2σ confidence interval shown as the shaded region.

27

Figure S33: Plot of non-deconvoluted 100 µM Cu^{II}-NTA pseudo-titration data performed with 35 (top row), 65 (middle row) and 95 (bottom row) µs mixing times. The non-deconvoluted experimental trace, background corrected data, and the validated distance distribution, are shown left-to-right respectively. The mean of the distance distribution is shown as the black trace, with the 2σ confidence interval shown as the shaded region.

Figure S34: Plot of non-deconvoluted 170 µM Cu^{II}-NTA pseudo-titration data performed with 32 (top row), 59 (middle row) and 86 (bottom row) µs mixing times. The non-deconvoluted experimental trace, background corrected data, and the validated distance distribution, are shown left-to-right respectively. The mean of the distance distribution is shown as the black trace, with the 2σ confidence interval shown as the shaded region.
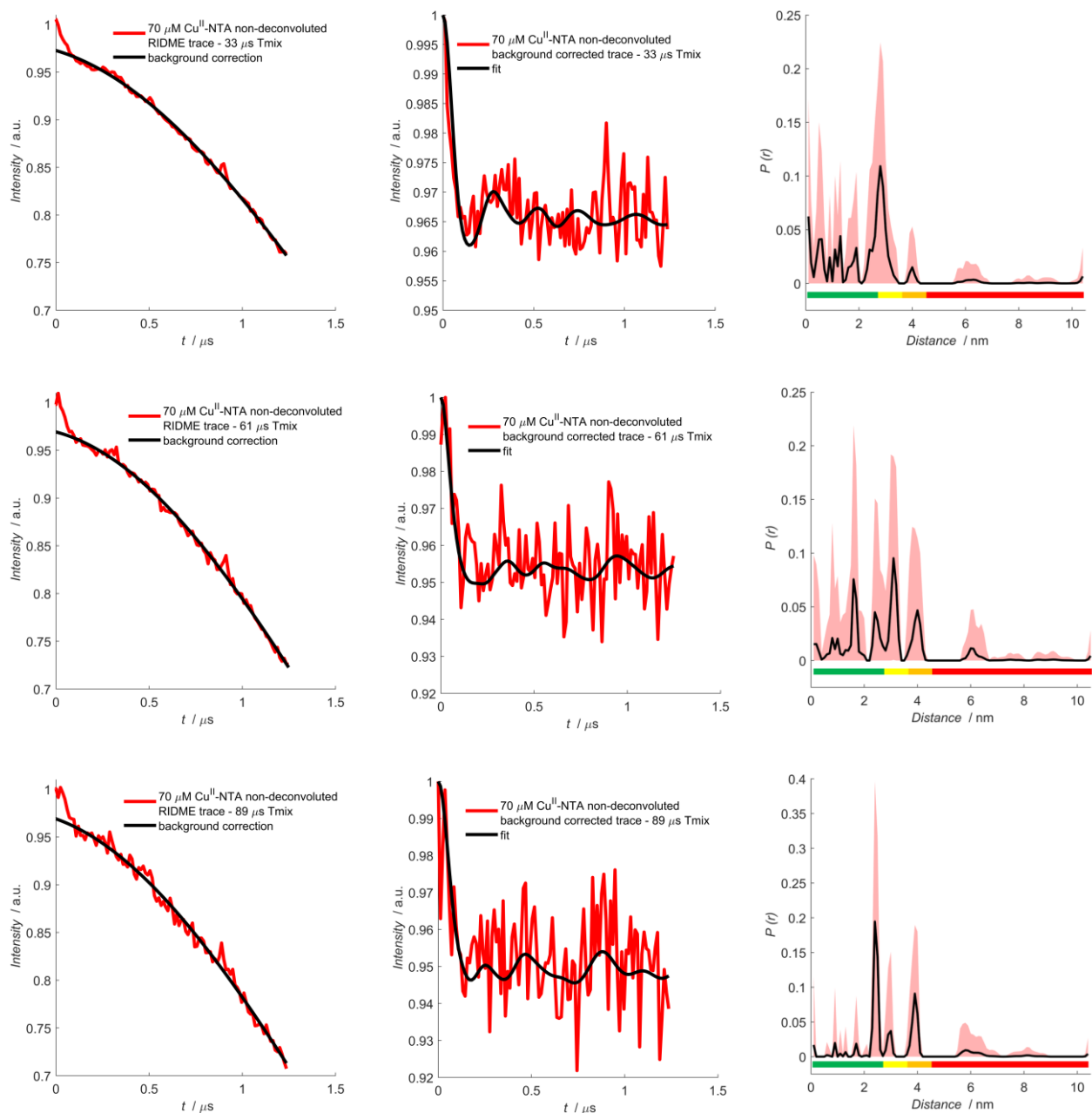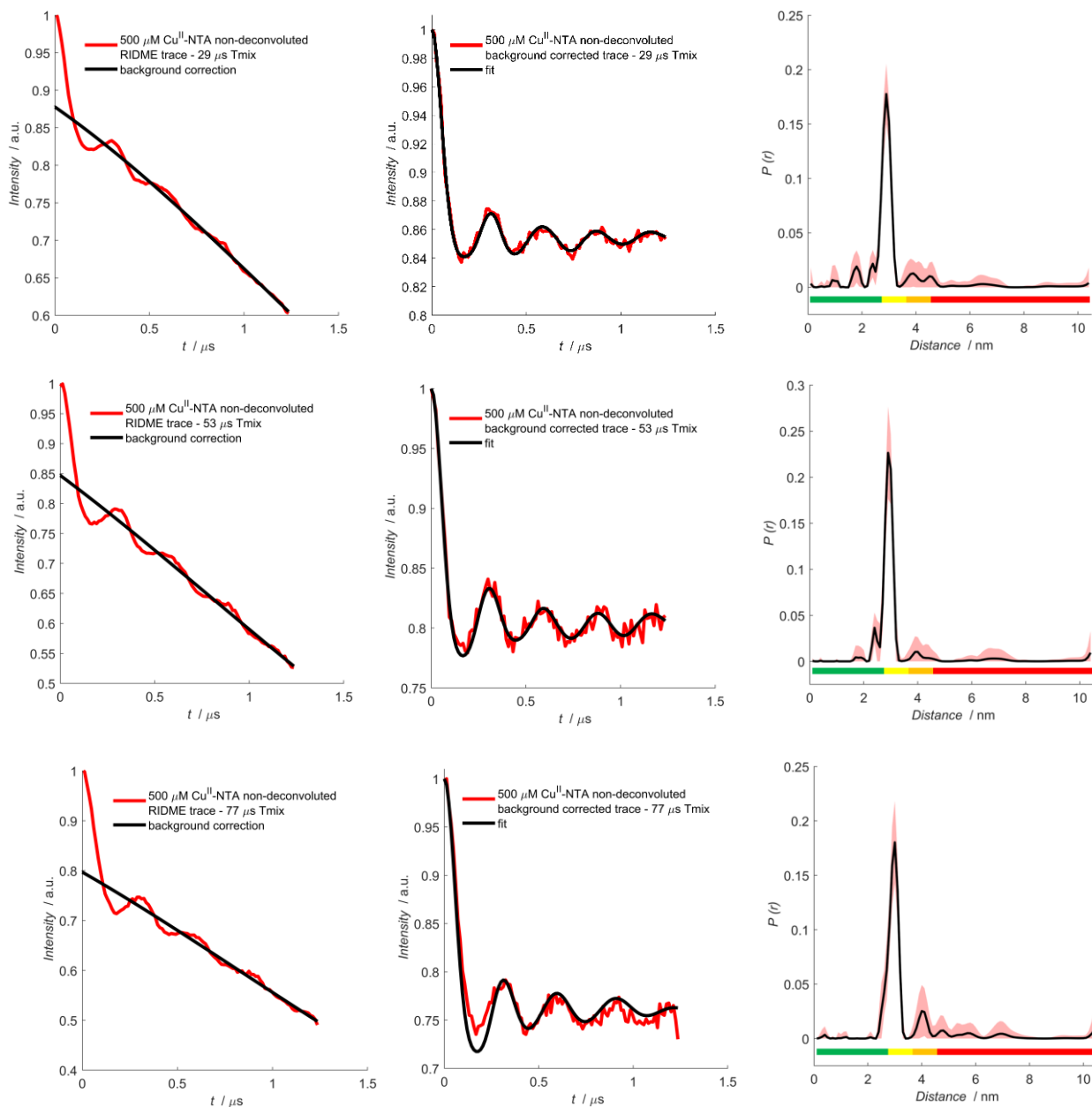
Figure S35: Plot of non-deconvoluted 500 µM Cu^{II}-NTA pseudo-titration data performed with 29 (top row), 53 (middle row) and 77 (bottom row) µs mixing times. The non-deconvoluted experimental trace, background corrected data, and the validated distance distribution, are shown left-to-right respectively. The mean of the distance distribution is shown as the black trace, with the 2σ confidence interval shown as the shaded region.
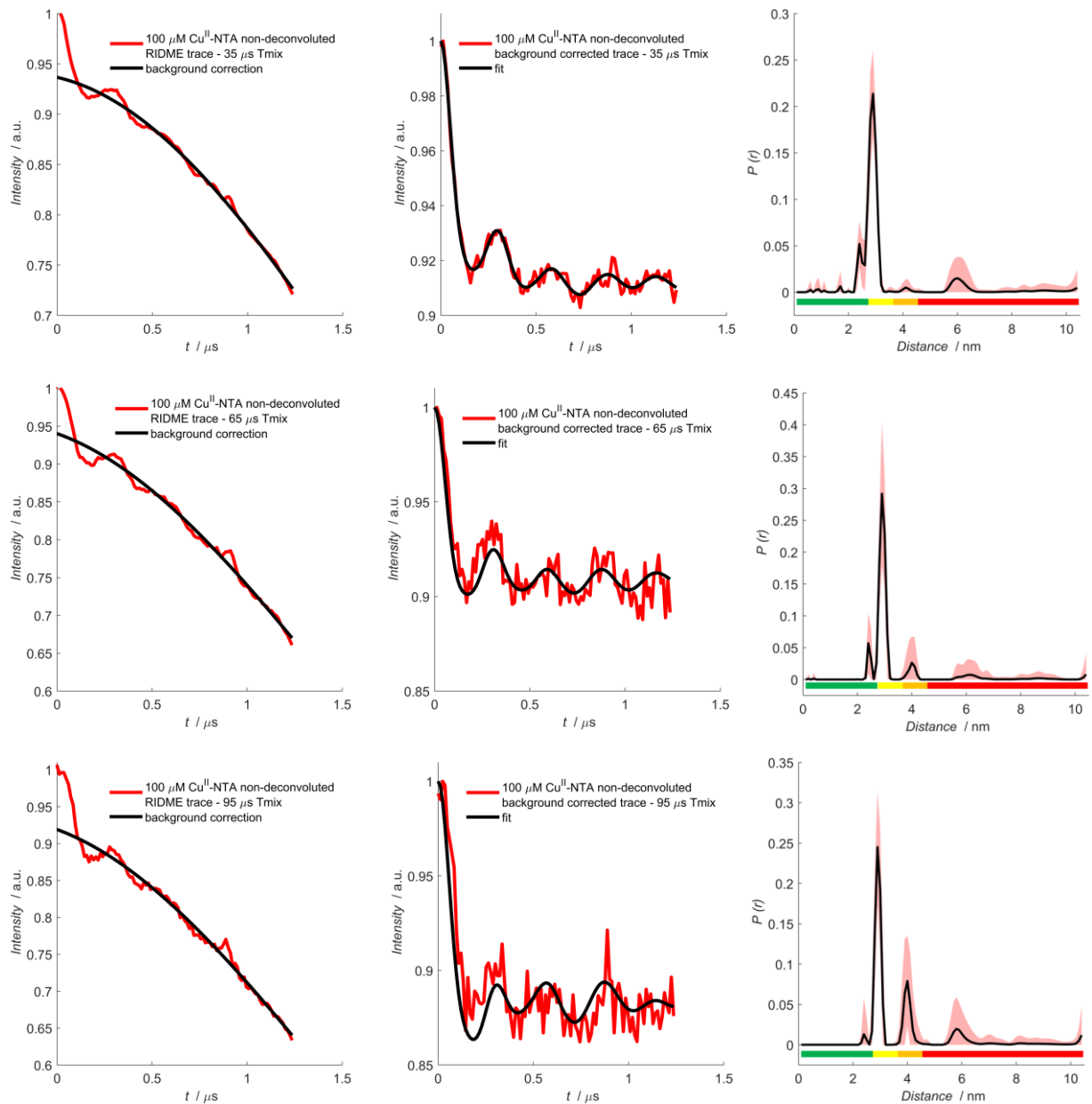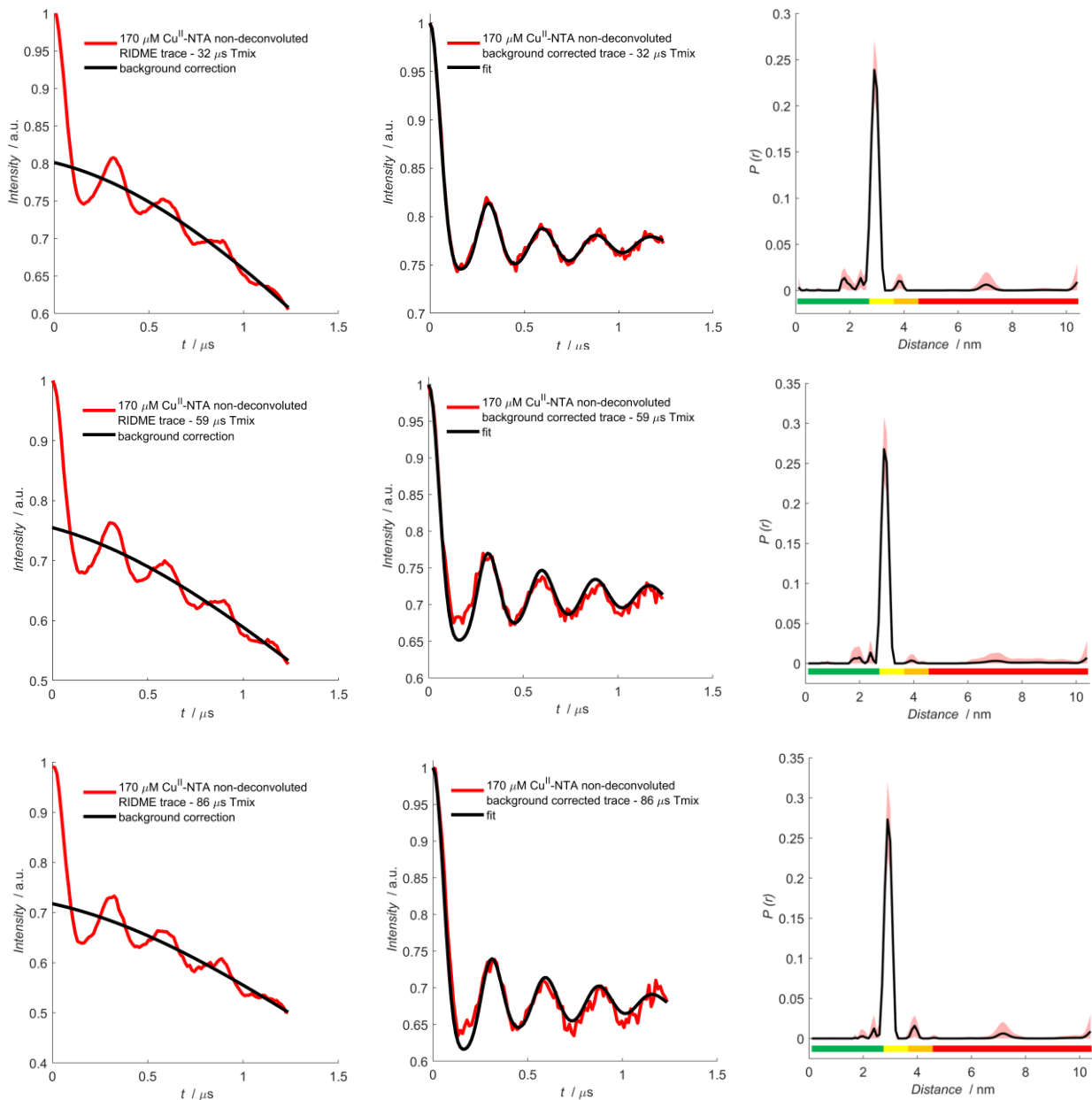
Figure S36: Plot of non-deconvoluted 1000 μM Cu^{II}-NTA pseudo-titration data performed with 24 (top row), 43 (middle row) and 62 (bottom row) μs mixing times. The non-deconvoluted experimental trace, background corrected data, and the validated distance distribution, are shown left-to-right respectively. The mean of the distance distribution is shown as the black trace, with the 2σ confidence interval shown as the shaded region.
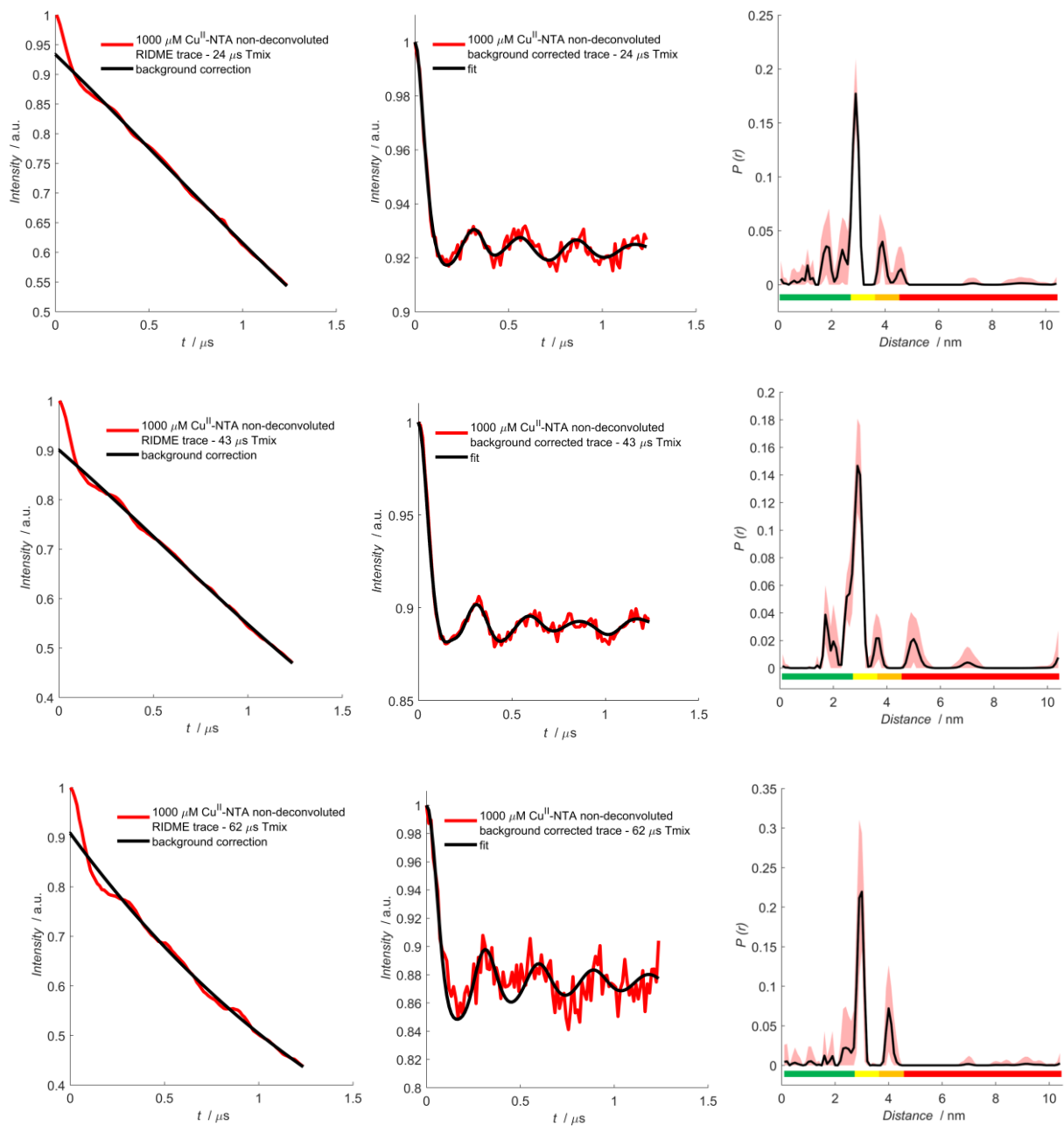
Background correction parameters and modulation depths for each sample are given overleaf in table S11.

Sample	Mixing time [µs]			Zero-time [ns]			Background Start [ns]			Background Cut-off [ns]			Δ		
100 µM 6H/8H/28H/32H + 50 µM Cu^{II}-NTA	35	65	95	219	-	241	283	-	239	1224	-	1200	$0.013 \pm 4.8 \times 10^{-3}$	-	$0.010 \pm 6.0 \times 10^{-3}$
100 µM 6H/8H/28H/32H + 70 µM Cu^{II}-NTA	33	61	89	211	203	213	106	150	327	1236	1248	1236	$0.027 \pm 5.4 \times 10^{-3}$	$0.031 \pm 7.0 \times 10^{-3}$	$0.031 \pm 6.4 \times 10^{-3}$
100 µM 6H/8H/28H/32H + 100 µM Cu^{II}-NTA	35	65	95	211	210	216	371	106	62	1236	1236	1236	$0.063 \pm 1.6 \times 10^{-2}$	$0.060 \pm 2.0 \times 10^{-2}$	$0.081 \pm 2.0 \times 10^{-2}$
100 µM 6H/8H/28H/32H + 170 µM Cu^{II}-NTA	32	59	86	208	207	209	106	283	194	1236	1236	1236	$0.199 \pm 2.4 \times 10^{-2}$	$0.245 \pm 2.6 \times 10^{-2}$	$0.282 \pm 3.4 \times 10^{-2}$
100 µM 6H/8H/28H/32H + 500 µM Cu^{II}-NTA	29	53	77	208	207	208	150	150	283	1236	1236	1236	$0.122 \pm 1.5 \times 10^{-2}$	$0.153 \pm 2.2 \times 10^{-2}$	$0.203 \pm 2.8 \times 10^{-2}$
100 µM 6H/8H/28H/32H + 1000 µM Cu^{II}-NTA	24	43	62	210	208	207	150	150	283	1236	1236	1236	$0.066 \pm 7.8 \times 10^{-3}$	$0.099 \pm 1.1 \times 10^{-2}$	$0.092 \pm 1.4 \times 10^{-2}$

Table S11: Comparison of background correction parameters for the validated non-deconvoluted RIDME traces, using a second-order polynomial background function, shown in figures S31-36. The error in modulation depth is ± 2σ.

For the 6H/8H/28H/32H GB1 RIDME traces corrected assuming a stretched exponential background decay shown in figures S25-S30, the validated distance distributions show that under conditions of low loading (50 and 70 µM Cu^{II}-NTA) even the main peak at ~2.5 nm is barely above the noise floor, since at all distances the lower estimate (shown as the unfilled space) has a probability density close to 0. This is also recapitulated for the RIDME traces corrected assuming a second-order polynomial background correction shown in figures S31-S36. Importantly, for all higher concentrations of Cu^{II}-NTA (except for 170 µM Cu^{II}-NTA) there is a second significant peak at ~4.0 nm. This suggests that under such Cu^{II}-NTA labelling conditions there is a non-specific interaction away from the double-histidine motifs, or this may reflect the formation of a Cu^{II}-templated dimer construct. However, the feature is largely suppressed under conditions of optimal labelling but is still present in the 100 µM Cu^{II}-NTA sample, which is inconsistent with the peak resulting from a non-specific binding event. More likely, it is an erroneous feature arising from poor labelling efficiency or low signal to noise ratio (SNR). While all samples give a significant peak at 2.5 nm, it should be apparent that only under conditions of optimal Cu^{II}-NTA labelling can the distance be uniquely identified. It is also interesting to note that modulation depth is consistently higher when using a stretched exponential model of background correction, compared to a second-order polynomial, but that the standard deviation of Δ is consistently larger for the latter background model.

Despite the poor reliability of the distance distributions for several of the 6H/8H/28H/32H GB1 pseudo-titration samples, all modulation depth distributions have 95% confidence intervals within ± 0.03 (to 2 decimal places) of the distribution means, suggesting modulation depth information can be extracted reliably. Furthermore, the modulation depths calculated from the validations appear largely robust against choice of background correction model. It is also worth noting that the standard deviation (σ) increases with mixing time as expected. This trend is harder to predict for propagation of the error in the modulation depth quotient, since at longer mixing times, the error in Δ_{Tmix} will decrease, despite the increased error in the empirical modulation depth owing to reduced sensitivity. This is discussed in more detail in the subsequent section.

2.7   Error Analysis of RIDME Pseudo-titrations and Modulation Depth Profiles:

Error analysis of the RIDME pseudo-titrations was performed as described above, to assess the reliability of the modulation depth profiles and K_D information extracted. As a benchmark, the previously reported Cu^{II}-NTA/nitroxide RIDME pseudo-titration series[12] was replotted as a function of Cu^{II}-NTA concentration, while indicating the ± 2σ error bars in the modulation depth quotients. The modulation depth profile and corresponding weighted fitted value of K_D are shown overleaf in figure S37. Importantly, the weighted fitted value of K_D is highly consistent with the value previously reported, within a factor 2. The gaussian approximation of the fitted one-dimensional inverse error surface as a function of K_D is also shown in figure S37 and indicates a weighted fitted K_D value of 232 ± 130 nM.
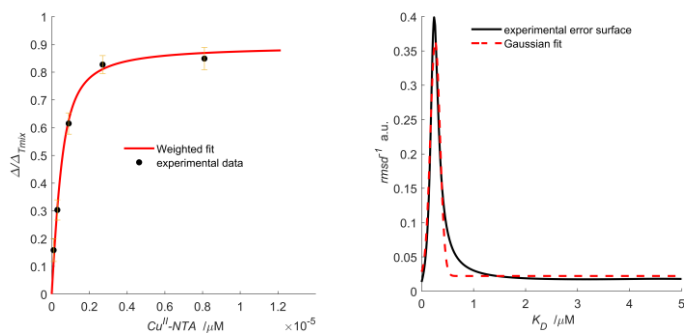
Figure S37: A weighted fitting of K_D, incorporating error bars for each experimental point. The weighted fitting is shown in the red trace, and the experimental data is shown in the black scatter (left). The reciprocal of the calculated root mean square deviation is shown as the black trace, and a fitted Gaussian of the data is shown in dotted red (right).

Applying this treatment to the tetra-histidine Cu^{II}-Cu^{II} RIDME pseudo-titrations is of interest, because as discussed in the main-text, relatively small errors in the estimation of T_1 can propagate a significant error in the calculation of Δ_{Tmix} for short mixing times. The modulation depth quotients and the associated errors for each T_1 and T_{mix} ratio are given below in tables S12-13, for stretched exponential and second-order polynomial background-correction models, respectively. It can be seen that the second-order polynomial background treatment slightly outperforms the stretched exponential background treatment, and yields systematically smaller errors in the modulation depth quotients; however errors are relatively consistent in each case, and typically reduce at longer mixing times, particularly for conditions of lower loading where sensitivity is limiting. Each series was fitted individually to determine the stability of the K_D values; weighted fittings of the individual series were also performed for comparison. Results are summarily shown below in figures S38-S39 for stretched exponential and second-order polynomial background-correction models, respectively. The unweighted- and weighted-fitted K_D values are given in tables S14-15, for stretched exponential and second-order polynomial background-correction models, respectively. It is observed that the K_D values differ by at least an order of magnitude in all cases, and only significantly deviate from expectation for the series recorded using a ratio of T_{mix} and T_1 of 0.7 This is as expected given that errors in modulation depth quotient are typically higher for these series.

Sample	Mixing time [µs]			$\Delta \times \Delta_{Tmix}^{-1}$		
100 µM 6H/8H/28H/32H + 50 µM Cu^{II}-NTA	35	65	95	$0.075 \pm 4.0 \times 10^{-2}$	-	$0.038 \pm 2.7 \times 10^{-2}$
100 µM 6H/8H/28H/32H + 70 µM Cu^{II}-NTA	33	61	89	$0.135 \pm 4.0 \times 10^{-2}$	$0.102 \pm 3.1 \times 10^{-2}$	$0.092 \pm 3.0 \times 10^{-2}$
100 µM 6H/8H/28H/32H + 100 µM Cu^{II}-NTA	35	65	95	$0.276 \pm 8.7 \times 10^{-2}$	$0.211 \pm 8.2 \times 10^{-2}$	$0.223 \pm 8.5 \times 10^{-2}$
100 µM 6H/8H/28H/32H + 170 µM Cu^{II}-NTA	32	59	86	$0.800 \pm 1.2 \times 10^{-1}$	$0.687 \pm 1.2 \times 10^{-1}$	$0.713 \pm 1.1 \times 10^{-1}$
100 µM 6H/8H/28H/32H + 500 µM Cu^{II}-NTA	29	53	77	$0.544 \pm 1.4 \times 10^{-1}$	$0.480 \pm 1.4 \times 10^{-1}$	$0.505 \pm 1.2 \times 10^{-1}$
100 µM 6H/8H/28H/32H + 1000 µM Cu^{II}-NTA	24	43	62	$0.356 \pm 6.5 \times 10^{-2}$	$0.355 \pm 6.7 \times 10^{-2}$	$0.234 \pm 9.6 \times 10^{-2}$

Table S12: Comparison of modulation depth quotients for series treated using a stretched exponential background function. The errors given in modulation depth quotient are ± 2σ.

Sample	Mixing time [µs]			$\Delta \times \Delta_{Tmix}^{-1}$		
100 µM 6H/8H/28H/32H + 50 µM Cu^{II}-NTA	35	65	95	$0.052 \pm 3.8 \times 10^{-2}$	-	$0.024 \pm 2.8 \times 10^{-2}$
100 µM 6H/8H/28H/32H + 70 µM Cu^{II}-NTA	33	61	89	$0.107 \pm 4.3 \times 10^{-2}$	$0.085 \pm 3.9 \times 10^{-2}$	$0.073 \pm 3.0 \times 10^{-2}$
100 µM 6H/8H/28H/32H + 100 µM Cu^{II}-NTA	35	65	95	$0.269 \pm 1.3 \times 10^{-1}$	$0.165 \pm 1.1 \times 10^{-1}$	$0.190 \pm 9.4 \times 10^{-2}$
100 µM 6H/8H/28H/32H + 170 µM Cu^{II}-NTA	32	59	86	$0.796 \pm 1.9 \times 10^{-1}$	$0.679 \pm 1.4 \times 10^{-1}$	$0.668 \pm 1.6 \times 10^{-1}$
100 µM 6H/8H/28H/32H + 500 µM Cu^{II}-NTA	29	53	77	$0.481 \pm 1.2 \times 10^{-1}$	$0.422 \pm 1.2 \times 10^{-1}$	$0.479 \pm 1.0 \times 10^{-1}$
100 µM 6H/8H/28H/32H + 1000 µM Cu^{II}-NTA	24	43	62	$0.261 \pm 6.2 \times 10^{-2}$	$0.276 \pm 6.1 \times 10^{-2}$	$0.220 \pm 6.7 \times 10^{-2}$

Table S13: Comparison of modulation depth quotients for series treated using a second-order polynomial background function. The errors given in modulation depth quotient are ± 2σ.
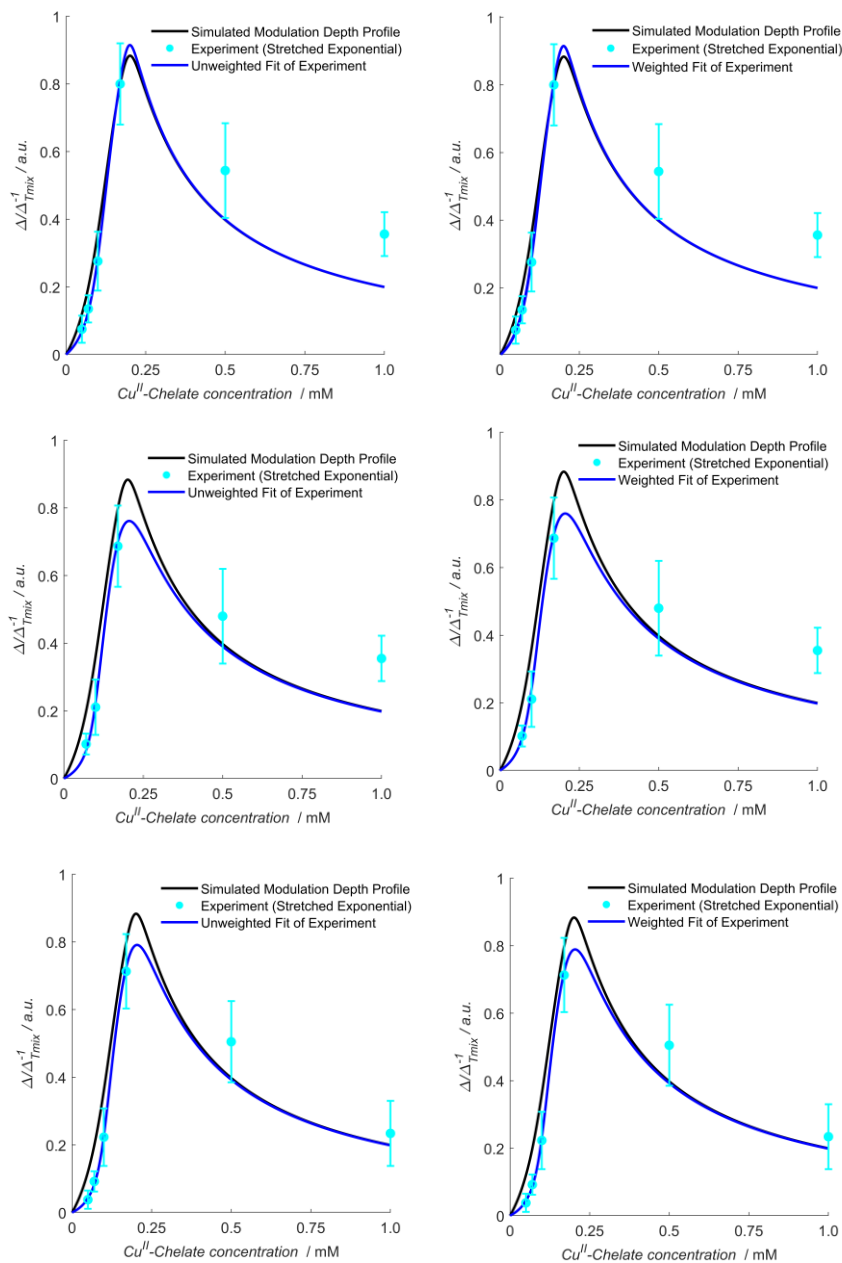
Figure S38: A comparative plot of the simulated modulation depth profile (black trace) and the corresponding unweighted (left) and weighted (right) fitted modulation depth profiles (blue traces) for each pseudo-titration series (background corrected using a stretched exponential function); ratios of 0.7, 1.3 and 1.9 between T_{mix} and T_1 are shown in the top, middle, and bottom rows respectively. Experimental data is also overlaid (cyan scatter), with the associated error bars.

Pseudo-titration Series	Ratio of T_{mix} and T_1	K_D Values
	[a.u.]	[μM]
Stretched Exponential Weighted Fit	0.7	0.76, 0.037
Stretched Exponential Unweighted Fit	0.7	0.76, 0.034
Stretched Exponential Weighted Fit	1.3	7.46, 0.229
Stretched Exponential Unweighted Fit	1.3	7.38, 0.184
Stretched Exponential Weighted Fit	1.9	5.56, 0.145
Stretched Exponential Unweighted Fit	1.9	5.42, 0.130

Table S14: Comparison of weighted and unweighted fitted K_D values estimated from pseudo-titration series treated using a stretched-exponential background function.
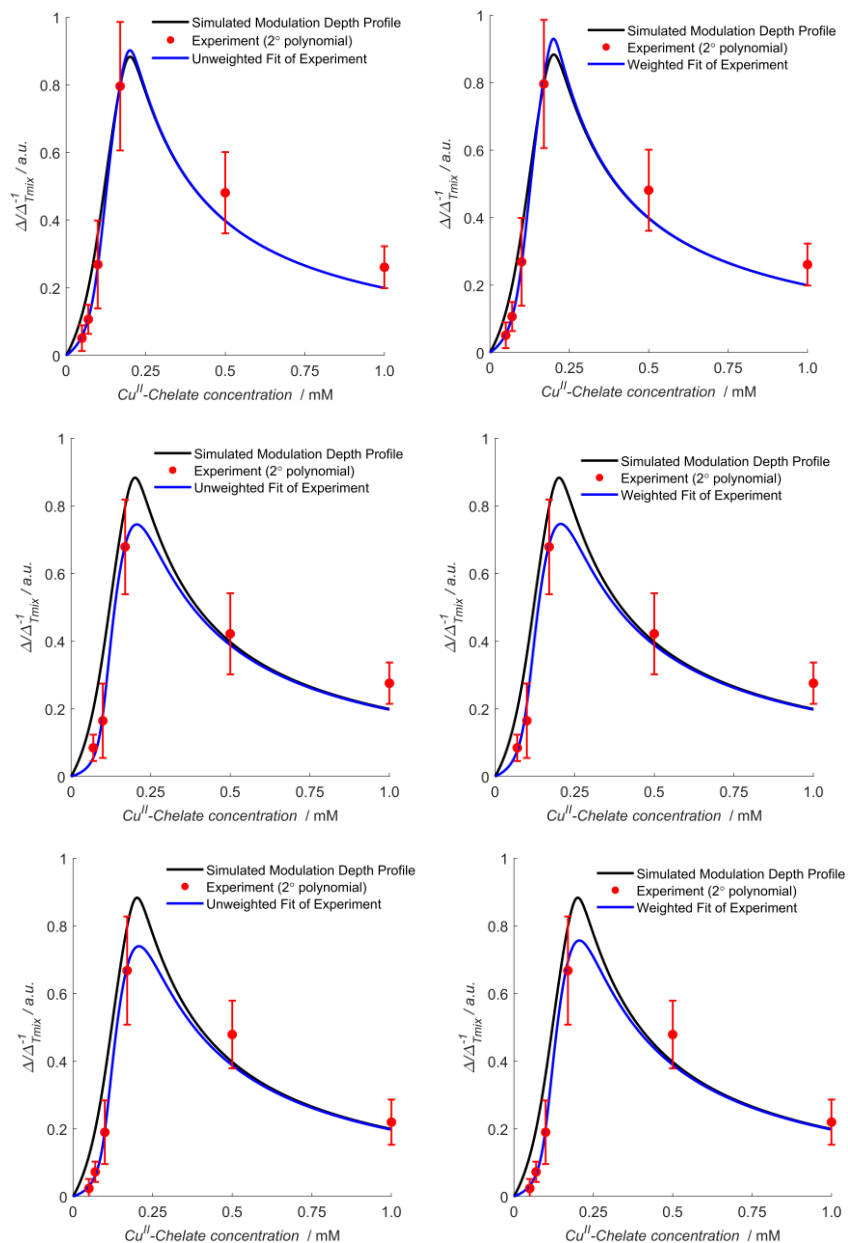
Figure S39: A comparative plot of the simulated modulation depth profile (black trace) and the corresponding unweighted (left) and weighted (right) fitted modulation depth profiles (blue traces) for each pseudo-titration series (background corrected using a second order polynomial function); ratios of 0.7, 1.3 and 1.9 between T_{mix} and T_1 are shown in the top, middle, and bottom rows respectively. Experimental data is also overlaid (red scatter), with the associated error bars.

Pseudo-titration Series	Ratio of T_{mix} and T_1 [a.u.]	K_D Values [µM]
Second Order Polynomial Weighted Fit	0.7	0.52, 0.018
Second Order Polynomial Unweighted Fit	0.7	1.0, 0.038
Second Order Polynomial Weighted Fit	1.3	8.5, 0.191
Second Order Polynomial Unweighted Fit	1.3	8.7, 0.130
Second Order Polynomial Weighted Fit	1.9	7.88, 0.145
Second Order Polynomial Unweighted Fit	1.9	9.11, 0.157

Table S15: Comparison of weighted and unweighted fitted K_D values estimated pseudo-titration series treated using a second-order polynomial background function.

Upon comparison of tables S14-15, it becomes apparent that the fitted pair of K_D values does not significantly change upon applying a weighting penalty to the experimental points. This is because the experimental points do not evenly influence the shape of the modulation depth profile, and this is especially true to the right of the maximum (see next section for detailed discussion). While the K_D values determined for the lowest ratio of T_{mix} and T_1 (0.7) are consistently lower than the expected K_D values, the pseudo-titration series recorded with higher ratios of T_{mix} and T_1 yield values that are largely consistent with expectation from previous work, and are in-line with the simultaneous fitting of all series; indicating an order of magnitude difference in relative affinities, with low µM and high nM affinities respectively. This was also reflected by the 2D error contours for each series (data shown below in figure S40).
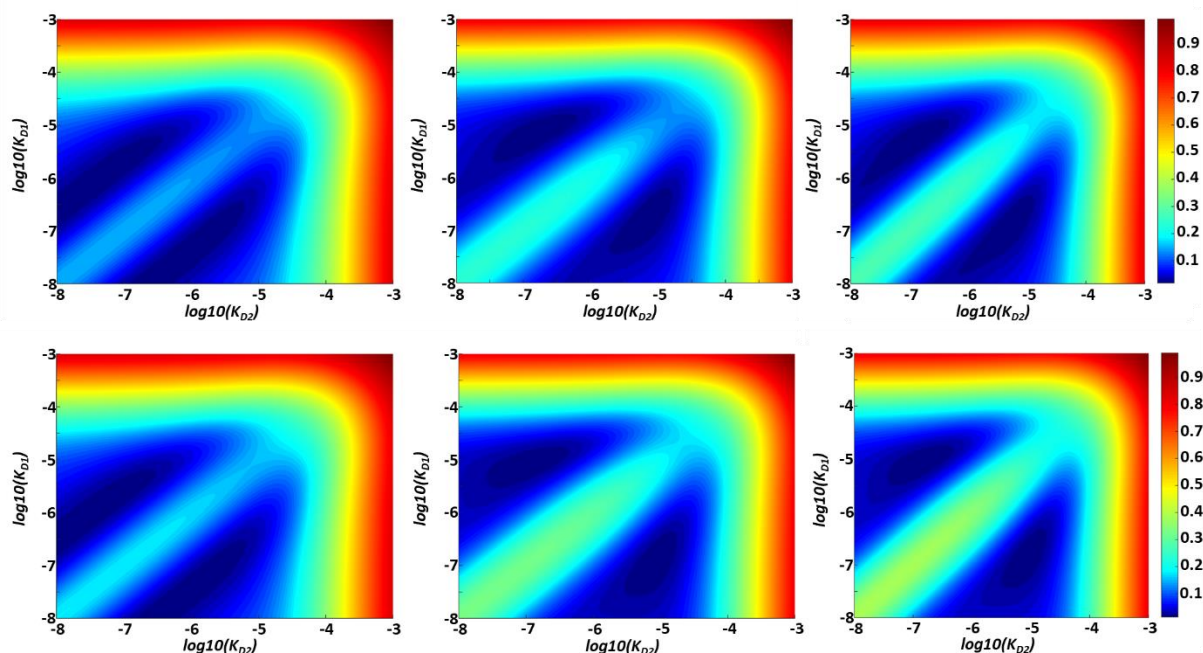

Figure S40: 2D error surfaces for the pseudo-titration series, using a stretched exponential background function (top row) or a second order polynomial background function (bottom row) and recorded with mixing times of 0.7, 1.3 and 1.9 x T_1 (left to right).

2.8   Exploratory Simulation of Modulation Depth Profiles:

To investigate the behaviour of modulation depth profiles under conditions of different concentration regimes for pairs of K_D values, exploratory simulations were performed for 100 µM protein, and K_D values of (100 µM, 100 nM), (10 µM, 100 nM), and (1 µM, 100 nM) shown in figure S41. This range of K_D values was chosen to demonstrate how this approach may be diagnostic of significant differences in affinity between the two sites. Notably, to the right of the maxima (the dH saturation point) addition of further Cu^{II}-chelate will lead to a reduction in the observed modulation depth quotient simply through a dilution effect. Therefore, this region of the curves does not add information about the K_D of the binding sites, but can act as an internal control for the sample Cu^{II}-chelate and protein concentration across the pseudo-titration series. Comparatively, to the left of the maxima (especially at low Cu^{II}-chelate concentrations) is shown to be more significant as a diagnostic of the respective magnitude and relative differences between affinities; in the case of a large difference (left panel, red trace), there is a lag in the initial rise of the modulation depth profile, which is recapitulated to a lesser extent as the relative difference reduces (left panel, black and blue traces).
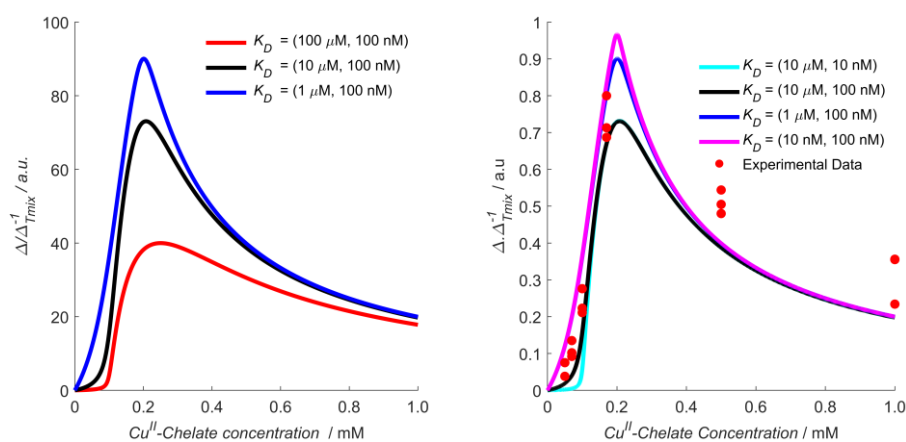
Figure S41: A comparative plot of modulation depth profiles simulated with 100 μM protein concentration and varying K_D values (indicated in the figure legends) (left), and an overlay of simulated profiles with experimental data (right). Note that these profiles are simulations rather than fits to the corresponding experimental data.

As expected, the modulation depth quotient at the maximum is highly sensitive to the respective magnitude of the K_D, and increasingly approaches unity as the overall affinity of the binding sites increases. Importantly, it should be noted that at sufficiently high affinities, the maximum of the modulation depth (under these simulated conditions) becomes the only distinguishing feature (see magenta trace in right panel), and protein concentration should be reduced to a regime with greater sensitivity to high affinities. From figure S41 it is also clear that the experimental data shown yields fitted K_D values of ~100 nM and ~5 μM, since observed values largely sit between the black and the blue simulated curves. This discussion indicates that these simulations may be useful in disentangling different binding modalities, given that the shape of the modulation depth profile can inform both the individual K_D values, and their relative difference in magnitude. This also explains why the error contours shown in the main text indicate that the pair of K_D values are not anti-correlated, because goodness-of-fit cannot be compensated by reduction of one K_D if the other increases.

Additionally, simulations were also performed for a fixed pair of K_D values and varying protein concentrations to investigate the influence on the position of the sensitivity maximum. One can identify two concentration regimes; i) the protein concentration exceeds the K_D values so that as ligand becomes available, binding to dH sites is quantitative, or ii) the protein concentration is below the K_D values, so that ligand binding is not quantitative. This can be related back to equation (34) in the main-text, and is reiterated here for clarity:

$$[L]_{1,2} = 2\theta_{1,2}[P]_0 \tag{S21}$$

In the first case, a sensitivity optimum is predicted at approximately $[L]_0 = 2[P]_0$ because ligand concentration is sufficiently high to drive quantitative binding to the protein molecule. In this case, the following approximation holds: $\theta_{1,2} = 1$, which implies complete saturation of the double-histidine motifs. In the second case, $\theta_{1,2} \neq 1$ because when $[L]_0 = 2[P]_0$, the ligand concentration is still insufficient to drive quantitative binding to the protein molecule. It follows that in the second case, a sensitivity optimum is predicted to occur at some ligand concentration: $[L]_0 > 2[P]_0$, which maximizes $\theta_{1,2}$. Results of the simulations given below in figure S42 for the high, and low protein concentration regimes, in the left and right panels, respectively. The predictions outlined above are borne-out by the simulations. The maxima of the modulation depth profiles are given in table S16. This suggests that this approach may be especially useful in studies where macromolecule concentrations are limiting, and where sensitivity optimisation is paramount.
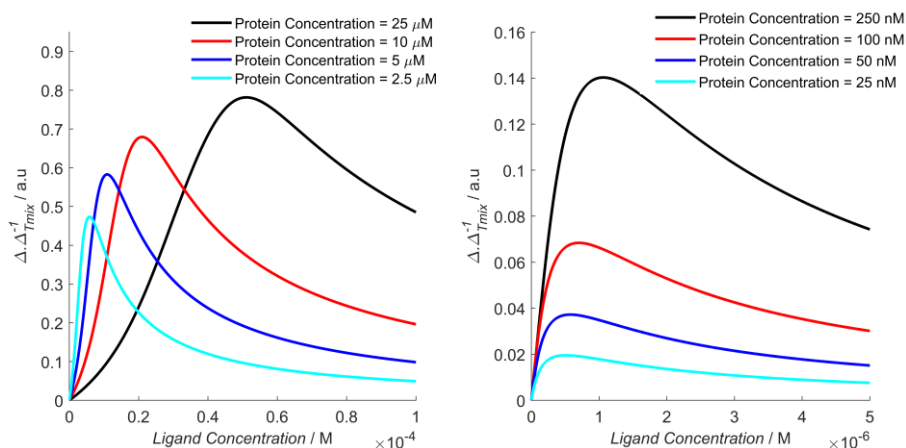
Figure S42: Comparative plots of modulation depth profiles simulated with varying protein concentrations (indicated in the figure legends) with K_D values of 140 nM, and 1.4 μM.

Protein Concentration [μM]	Label Concentration at Sensitivity Maximum [μM]
25	51
10	21
5.0	11
2.5	5.9
2.5×10^{-1}	1.1
1.0×10^{-1}	7.0×10^{-1}
5.0×10^{-2}	5.6×10^{-1}
2.5×10^{-2}	4.9×10^{-1}

Table S16: Comparison of sensitivity maxima positions for different simulated modulation depth profiles in figure S42.

2.9   Global Fit of All Cu^{II}-Cu^{II} RIDME Modulation Depth Profiles:

To check the stability of the fitted results for each of the individual mixing time series, all series were also fitted globally, with the expectation that the fitting should be reflective of the series recorded with the highest T_{mix} to T_1 ratio, since this should give the highest accuracy for K_D determination. Indeed, from the results shown below in figure S43, it is seen that the global fitting leads to K_D estimates which are closely aligned with those fitted from the individual series, recorded with a mixing time of $1.9 \times T_1$. Estimates of K_D from the global fitting are given below in table S17.
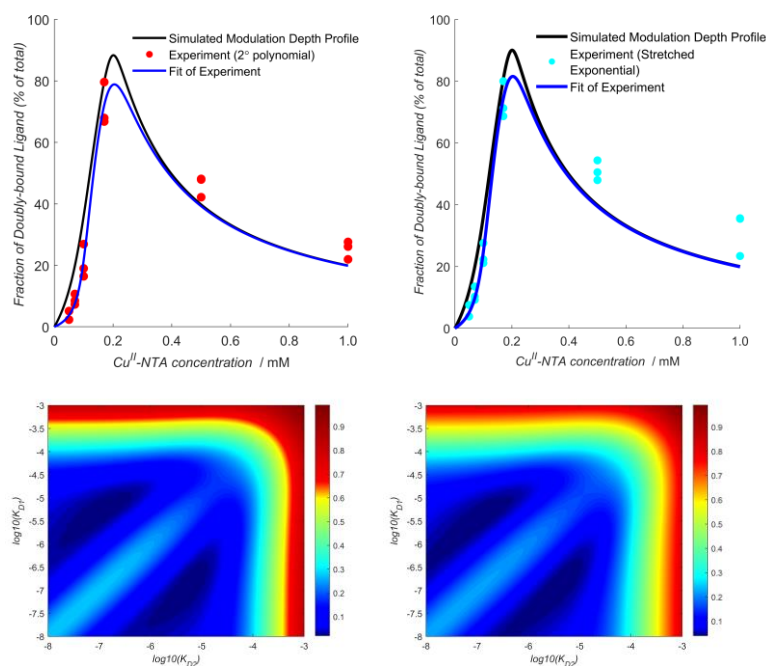
Figure S43. Top left) The experimental modulation depth quotients calculated using a second order polynomial background correction (red scatter), overlaid with the predicted modulation depth profile (black trace) and the associated fitted bivariate error function (blue trace). Top right) The experimental modulation depth quotients calculated using a stretched exponential background correction (cyan scatter), overlaid with the predicted modulation depth profile (black trace) and the associated fitted bivariate error function (blue trace). Bottom left) An error contour of the bivariate fitting of each dissociation constant to the experimental data shown in top left. Each dissociation constant varies 5 orders of magnitude from 10 nM to 1 mM. Bottom right) An error contour of the bivariate fitting of each dissociation constant to the experimental data shown in top right (same as the panel d) in figure 3 of the main text).

Pseudo-titration Series	K_D Values [µM]
Second Order Polynomial Background Model	0.126, 5.6
Stretched Exponential Background Model	0.127, 4.0

Table S17: Comparison of fitted K_D values estimated from pseudo-titration series treated using a second-order polynomial, and stretched exponential background function, respectively.

In the interest of completeness, a global fitting of both Cu^{II}-Cu^{II} RIDME and previously obtained Cu^{II}-nitroxide RIDME pseudo-titration series was performed, to determine if pseudo-titrations could be fitted globally, and used conjunctively. Results of this combined fitting approach are shown in figure S44 below and indicate that there are minimal changes to the fitted values from the Cu^{II}-Cu^{II} RIDME alone. This could lead one to suggest that using Cu^{II}-Cu^{II} RIDME is preferable to Cu^{II}-nitroxide RIDME, as it accesses more information than the latter approach, with respect to binding equilibria studies. However, the consistency of the global fitting across all series instils some faith as to the reliability of the K_D estimates.
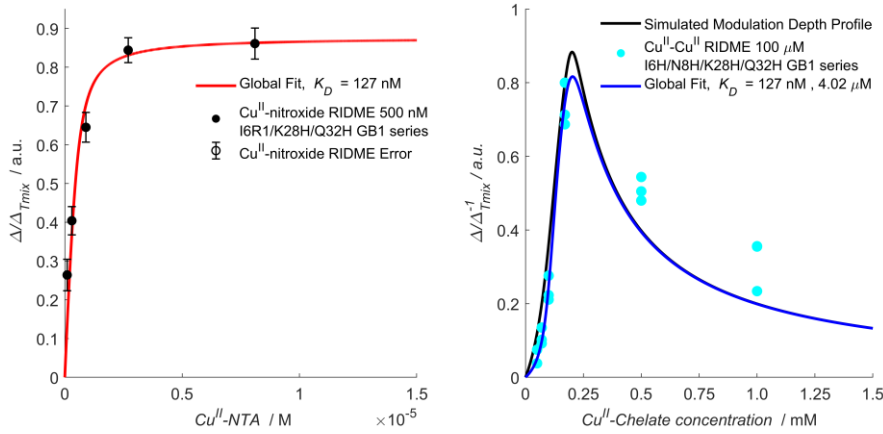
Figure S44: A global fit of both Cu^{II}-nitroxide and Cu^{II}-Cu^{II} RIDME pseudo-titrations shown in the left and right panels, respectively.

Additionally, it should be noted that the pseudo-titrations performed at 25 and 75 µM protein concentration in the previous work[12] were not included in the globally fitted K_D values. Rationale for omission of these series is provided in figure S45, comparison of the error surfaces as a function of K_D showcases that only the 500 nM protein concentration series gives an unambiguous global minimum. The steepness of the error surface can be further contextualised as the resolution of the fitted hyperbolic function curvature, for a one-site Langmuir isotherm. Indeed, it was noted in the previous work that at all higher protein concentrations, the hyperbolic function behaved as a step function, making unambiguous estimation of the K_D difficult.
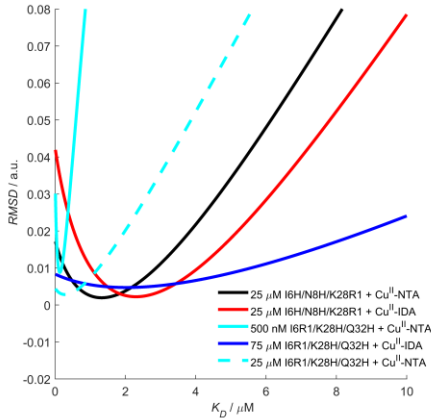

Figure S45: A comparison of the 1D error surfaces of the fitted pseudo-titrations performed at 500 nM, 25 and 75 µM GB1 protein concentrations, in presence of Cu^{II}-NTA and Cu^{II}-IDA. Notice that only the 500 nM concentration series (solid cyan) yields an unambiguous global minimum.

2.10   Influence of a Bi-exponential Approximation of T_1 on Modulation Depth Quotients:

As described in the main text, under the mono-exponential approximation of T_1, the asymptotic limit of modulation depth for a given ratio of mixing time (T_{mix}) and T_1, Δ_{Tmix} is defined by equation S22:

$$\Delta_{Tmix} = \left(\frac{\left(1 - exp\left(\frac{-T_{mix}}{T_1}\right)\right)}{2} \right) \tag{S22}$$

Under the bi-exponential approximation of T_1 this can be rewritten as:

$$\Delta_{Tmix} = \left(\frac{\left(1 - \left[b \times exp\left(\frac{-T_{mix}}{T_1^{fast}}\right) + (1-b) \times exp\left(\frac{-T_{mix}}{T_1^{slow}}\right)\right]\right)}{2} \right) \tag{S23}$$

40

where: $T_1{}^{fast}$ and $T_1{}^{slow}$ are the fast and slow components of the bi-exponential, and b is the weighted contribution of the fast component. Therefore, the bi-exponential approximation of T_1 influences the modulation depth quotient, and results are given for quotients of the 6H/8H/28H/32H GB1 pseudo-titration series under the mono- and bi-exponential approximations of Δ_{Tmix}, in tables S18 and S19, respectively. It is observed that the modulation depth quotients appear relatively stable regardless of the model used to approximate the T_1. This is consistent with strongly mono-exponential longitudinal relaxation behaviour across the pseudo-titration series, and is further confirmed upon comparison of the 1/e and 1/e^2 times, in tables S1 and S2. However, under the mono-exponential approximation of T_1 the modulation depth quotients are typically higher, particularly for shorter mixing times, primarily because the fast component is overfitted under this approximation. When the fast component is appropriately weighted under the bi-exponential approximation, the modulation depth quotient reduces.

Sample	Mixing time [µs]			$\Delta \times \Delta_{Tmix}{}^{-1}$ (mono-exponential)		
100 µM 6H/8H/28H/32H + 50 µM Cu^{II}-NTA	35	65	95	0.075	-	0.038
100 µM 6H/8H/28H/32H + 70 µM Cu^{II}-NTA	33	61	89	0.135	0.102	0.092
100 µM 6H/8H/28H/32H + 100 µM Cu^{II}-NTA	35	65	95	0.276	0.211	0.223
100 µM 6H/8H/28H/32H + 170 µM Cu^{II}-NTA	32	59	86	0.800	0.687	0.713
100 µM 6H/8H/28H/32H + 500 µM Cu^{II}-NTA	29	53	77	0.544	0.480	0.505
100 µM 6H/8H/28H/32H + 1000 µM Cu^{II}-NTA	24	43	62	0.356	0.355	0.234

Table S18: Modulation depth quotients for 6H/8H/28H/32H GB1 pseudo-titration series treated using a stretched exponential background function, and assuming a mono-exponential treatment of T_1 and Δ_{Tmix}.

Sample	Mixing time [µs]			$\Delta \times \Delta_{Tmix}{}^{-1}$ (bi-exponential)		
100 µM 6H/8H/28H/32H + 50 µM Cu^{II}-NTA	35	65	95	0.072	-	0.038
100 µM 6H/8H/28H/32H + 70 µM Cu^{II}-NTA	33	61	89	0.129	0.101	0.093
100 µM 6H/8H/28H/32H + 100 µM Cu^{II}-NTA	35	65	95	0.264	0.210	0.226
100 µM 6H/8H/28H/32H + 170 µM Cu^{II}-NTA	32	59	86	0.764	0.705	0.691
100 µM 6H/8H/28H/32H + 500 µM Cu^{II}-NTA	29	53	77	0.500	0.469	0.509
100 µM 6H/8H/28H/32H + 1000 µM Cu^{II}-NTA	24	43	62	0.322	0.343	0.234

Table S19: Modulation depth quotients for 6H/8H/28H/32H GB1 pseudo-titration series treated using a stretched exponential background function, and assuming a bi-exponential treatment of T_1 and Δ_{Tmix}.

For completeness, calculated modulation depth quotients, under the bi-exponential approximation of T_1, were fitted to a pair of dissociation constants and the results were compared with the values determined under the mono-exponential approximation. Fits are shown in figure S46 and K_D values determined under the mono- and bi-exponential approximation of T_1, are given in columns 2 and 3 of table S20, respectively. Comparison shows that the variability of K_D values across the different ratios of T_{mix} to T_1 is lower when using the bi-exponential approximation.
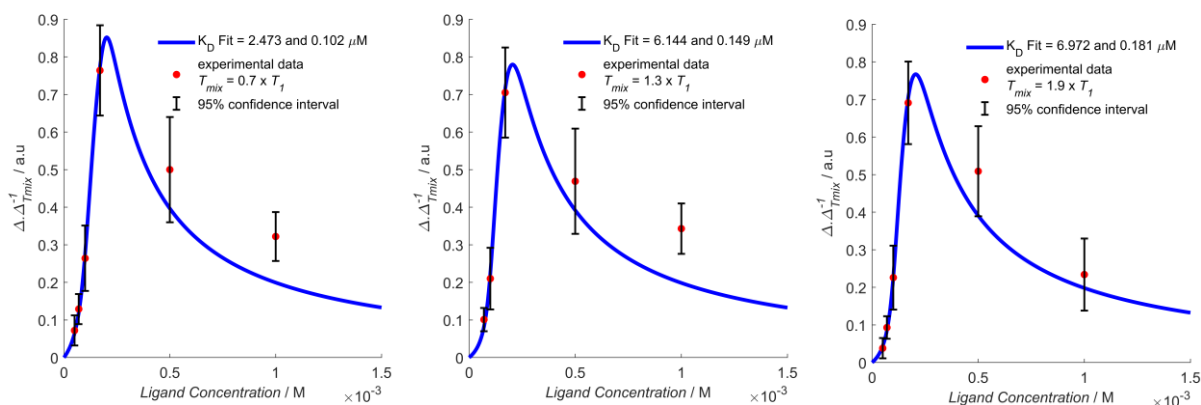

Figure S46: Fits of the experimental pseudo-titrations under the bi-exponential approximation of T_1 for different ratios of mixing time and T_1.

Ratio of T_{mix} and T_1 [a.u.]	Fit K_D values (mono-exponential) [µM]	Fit K_D values (bi-exponential) [µM]
0.7	0.76, 0.034	2.47, 0.102
1.3	7.38, 0.184	6.14, 0.149
1.9	5.42, 0.130	6.97, 0.181

Table S20: K_D values estimated from modulation depth quotients for different ratios of mixing time and T_1 calculated using a mono- and bi-exponential treatment of T_1, in the second and third columns, respectively.

III   References:

1   S. Milikisyants, F. Scarpelli, M. G. Finiguerra, M. Ubbink, and M. Huber, *J. Magn. Reson.,* 2009, **201**, 48.

2   M. Pannier, S. Veit, A. Godt, G. Jeschke, and H. W. Spiess, *J. Magn. Reson.*, 2000, **142**, 331.

3   K. Keller, A. Doll, M. Qi, A. Godt, G. Jeschke, and M. Yulikov, *J. Magn. Reson.*, 2016, **272**, 108.

4   I. Ritsch, H. Hintz, G. Jeschke, A. Godt and M. Yulikov, *Phys. Chem. Chem. Phys*., 2019, **21**, 9810.

5   K. Keller, Q. Mian, C. Gmeiner, I. Ritsch, A. Godt, G. Jeschke, A. Savitsky, and M. Yulikov, *Phys. Chem. Chem. Phys*., 2019, **21**, 8228.

6   S. G. Worswick, J. A. Spencer, G. Jeschke, and I. Kuprov, *Sci. Adv.,* 2018, **4**, 5218.

7   D. Abdullin, and O. Schiemann, *Chempluschem*, 2020, **85**, 353.

8   K. Ackermann, C. Pliotas, S. Valera, J. H. Naismith, and B. E. Bode, *Biophys. J.* 2017, **113**, 1968.

9   H. H. Ku, *J. Res. Natl. Bur. Stand.*, 1966, **4**, 262.

10   K. Singewald, X. Bogetti, K. Sinha, G. S. Rule, S. Saxena, *Angew. Chem. Int. Ed.,* 2020, DOI: https://doi.org/10.1002/anie.202009982.

11   S. Stoll, A. Schweiger, *J. Magn. Reson.* 2006, **178**, 42.

12   J. L. Wort, K. Ackermann, A. Giannoulis, A. J. Stewart, D. G. Norman, and B. E. Bode, *Angew. Chem. Int. Ed.,* 2019, **58**, 11681.